Static and free-vibration analyses of cracks in thin-shell structures based on an isogeometric-meshfree coupling approach

Nhon Nguyen-Thanh*, Weidong Li, Kun Zhou*

School of Mechanical and Aerospace Engineering, Nanyang Technological University, 50 Nanyang Avenue, Singapore 639798, Singapore

Abstract

This paper develops a coupling approach which integrates the meshfree method and isogeometric analysis (IGA) for static and free-vibration analyses of cracks in thin-shell structures. In this approach, the domain surrounding the cracks is represented by the meshfree method while the rest domain is meshed by IGA. The present approach is capable of preserving geometry exactness and high continuity of IGA. The local refinement is achieved by adding the nodes along the background cells in the meshfree domain. Moreover, the equivalent domain integral technique for three-dimensional problems is derived from the additional Kirchhoff-Love theory to compute the J-integral for the thin-shell model. The proposed approach is able to address the problems involving through-the-thickness cracks without using additional rotational degrees of freedom, which facilitates the enrichment strategy for crack tips. The crack tip enrichment effects and the stress distribution and displacements around the crack tips are investigated. Free vibrations of cracks in thin shells are also analyzed. Numerical examples are presented to demonstrate the accuracy and computational efficiency of the coupling approach.

Keywords: Isogeometric Analysis, Meshfree Method, Thin shell, Fracture Mechanics, Reproducing Conditions, Coupling approach

1. Introduction

Shell structures are widely used in civil, mechanical, aerospace and marine engineering applications. Compared with three-dimensional (3D) formulations, a shell-type formulation limits the number of degrees of freedom (DOF) in an elegant manner, leading to a reasonable computational cost while keeping a good accuracy. A variety of shell elements have been developed, which can be classified by the thickness of the shell and the curvature of the mid-surface [1, 2, 3]. Depending on the thickness, shell elements can be categorized into thin-shell elements [4, 5, 6, 7, 8] and thick-shell elements [9, 10, 11, 12, 13]. Thick-shell elements are based on the Reissner-Mindlin theory which requires only the C^0-continuity for the deflection and rotation fields. Thin-shell elements are based on the Kirchhoff-Love (KL) theory [14] that requires the C^1-continuity of the displacement field, and the transverse shear deformations are negligible. The thin-shell KL theory requires the approximation of the deformation to have the second-order derivatives which are square integrable.

*Corresponding authors. Email addresses: thanhnhon@ntu.edu.sg (Nhon Nguyen-Thanh), kzhou@ntu.edu.sg (Kun Zhou)

The use of the higher-order continuity in the context of thin-shell analysis eliminates the need for rotational DOF or the additional discretization.

The meshfree methods are viewed as next-generation computational techniques for problems involving large deformation, fracture and fragmentation. Since the meshfree methods do not rely on a fixed topological connectivity between nodes, they are expected to be more adaptive and robust in handling the problems where the classic grid-based methods are not suitable [15, 16, 17, 18, 19]. Many types of meshfree methods have been developed, such as the smooth particle hydrodynamic method [20], the element-free Galerkin method [21], and the reproducing kernel particle method (RKPM) [22, 23, 24, 25]. For fracture analysis, compared to the traditional finite element method (FEM), the meshfree methods are able to save much computational time by avoiding re-meshing after each crack extension [26, 27, 28, 29]. However, the meshfree method usually has less computational efficiency than the FEM, as more computational cost is required in the meshfree interpolation and numerical integration.

The isogeometric analysis (IGA) [30] has been proposed for the problems governed by partial differential equations. Design and analysis can be integrated seamlessly by directly adopting the functions generated by CAD programs as the basis functions in the context of IGA. The non-uniform rational B-splines (NURBS) which are widely used in CAD models are not only applicable to engineering analysis but also capable of delivering accuracy superior to standard FEM for many applications [31, 32, 33, 34**?** , 35, 36, 37, 38]. Taking advantages of extended FEM (XFEM) and IGA, extended IGA (XIGA) has been developed for fracture analysis [39, 40, 41, 42, 43, 44]. However, IGA based on NURBS imposes rigidity on volume meshing, which requires special technique to accommodate trimmed surfaces, local refinement or in-congruent surface descriptions at the opposing faces.

In order to generate coupled approximation spaces with higher-order smoothness, several approaches have recently been proposed to couple IGA and meshfree methods discretizations. Wang and Zhang [45] developed a coupled IGA-meshfree method in which the NURBS basis functions and RKPM shape functions were combined based on the consistency conditions. Rosolen *et al.* presented a method to integrate the local maximum entropy meshfree method with the IGA method based on the reproducibility conditions [46]. The volume discretization was usually challenging for IGA, whereas it can be readily solved by meshfree methods. Valizadeh *et al.* [47] proposed the method that combines the IGA with the RKPM in the physical domain. In this way, the basis functions can be constructed directly in the physical domain without requiring the global geometry parameterization. Recently, Zhang and Wang *et al.* [48] presented a reproducing kernel formulation for NURBS which provides a reliable meshfree strategy to the local refinement in IGA. Also, the analysis of two-dimensional crack problems have been introduced based on the IMF coupling approach [49].

In this paper, we develop an isogeometric-meshfree coupling approach (IMF) for the static and free-vibration analyses of cracks in thin-shell structures. The approach divides the physical domain into two sub-domains which are formulated with the IGA and meshfree methods, respectively. The meshfree method is adopted for the sub-domain containing cracks, and the IGA basis functions are employed for the domains away from the cracks. By taking advantages of IGA and meshfree methods, the present approach is capable of preserving geometry exactness and achieving local refinement flexibility, which helps to avoid meshing and aligning the element boundaries to the crack faces. The local refinement strategy can be the same as that of the meshfree methods in which field nodes are directly inserted without pre-defining the nodal connectivity. Moreover, the

equivalent domain integral technique for 3D problems is derived for thin-shell models based on the KL-theory to compute the J-integral. The proposed approach is not only able to address the problems involving through-the-thickness cracks, but also avoids the use of additional rotational DOF, which facilitates the enrichment strategy for crack tips. The stress intensity factors (SIFs) are also formulated based on the interaction integral. Furthermore, the crack tip enrichment effects, the stress distribution and the displacements are investigated.

The structure of this paper is as follows. Section 2 introduces the meshfree and isogeometric approximations which are based on the moving least squares (MLS) shape functions and the NURBS basis functions, respectively. Section 3 presents the isogeometric and meshfree coupling approach within the framework of reproducing conditions. The thin-shell formulation is derived in Section 4. The crack modeling and applying enrichment functions in IMF are described in Section 5. Thereafter, the robustness and efficiency of the proposed approach are illustrated in Section 6. Finally, the conclusions are given in Section 7.

2. Isogeometric and meshfree approximations

Two approximation functions, the NURBS basis functions and the MLS shape functions, are described in this section. A consistent approximation is implemented in the parametric domain for the IMF coupling approach.

2.1. Isogeometric approximation

The B-spline basis functions $N_{i,p}(\xi)$ of order $q = 0$ (piece-wise constant) are defined recursively on the corresponding knot vector as follows:

$$N_{i,q}(\xi) = \begin{cases} 1 & \text{if } \xi_i \leq \xi \leq \xi_{i+1} \\ 0 & \text{otherwise} \end{cases} , \tag{1}$$

$$N_{i,q}(\xi) = \frac{\xi - \xi_i}{\xi_{i+q} - \xi_i} N_{i,q-1}(\xi) + \frac{\xi_{i+q+1} - \xi}{\xi_{i+q+1} - \xi_{i+1}} N_{i+1,q-1}(\xi) \quad (\text{for q} \geq 1) . \tag{2}$$

As for the B-spline surface, it can be expressed as

$$\mathbf{S}(\xi, \eta) = \sum_{i=1}^{n} N_i(\xi, \eta) \mathbf{P}_i , \tag{3}$$

where $\mathbf{P}_i$ are the control points in a bidirectional control net and $N_i(\xi, \eta)$ are the B-spline basis functions.

Therefore, the NURBS surface can be defined in a similar way to the B-spline surface by multiplying basis functions and weights w_i as follows:

$$\mathbf{S}(\xi, \eta) = \sum_{i=1}^{n} R_i(\xi, \eta) \mathbf{P}_i ; \quad R_i = \frac{N_i(\xi, \eta) w_i}{\sum_{\bar{i}=1}^{n} N_{\bar{i}}(\xi, \eta) w_{\bar{i}}} . \tag{4}$$

2.2. Meshfree approximation

The MLS shape function is widely used in mehsfree methods [50]. Based on the combination of a set of field nodes that are discretely distributed in a domain $\mathbf{\Omega}$, the meshfree approximation

$u^h(\boldsymbol{\xi})$ of the displacement function $u(\boldsymbol{\xi})$ can be expressed as follows:

$$u^h(\boldsymbol{\xi}) = \sum_{J=1}^{m} p_J(\boldsymbol{\xi})\, a_J(\boldsymbol{\xi}) = \mathbf{p}^{\mathrm{T}}(\boldsymbol{\xi})\, \mathbf{a}(\boldsymbol{\xi}), \tag{5}$$

where $\mathbf{p}(\boldsymbol{\xi})$ are the polynomial basis functions, $\boldsymbol{\xi} = [\xi, \eta]^T$ are the parametric coordinates, m is the number of basis functions and $\mathbf{a}(\boldsymbol{\xi})$ are the vector coefficients.

A 2D polynomial basis function of order q is defined as follows:

$$\mathbf{p}(\boldsymbol{\xi}) = \left\{1, \xi, \eta, \xi^2, \xi\eta, \eta^2, \cdots, \xi^q, \cdots, \eta^q\right\}^{\mathrm{T}}. \tag{6}$$

This coupling approach utilizes the linear, quadratic and cubic polynomial basis functions which are given as follows:

$$\mathbf{p}(\boldsymbol{\xi}) = \begin{cases} \{1, \xi, \eta\}^{\mathrm{T}} & (q=1) \\ \left\{1, \xi, \eta, \xi^2, \xi\eta, \eta^2\right\}^{\mathrm{T}} & (q=2) \\ \left\{1, \xi, \eta, \xi^2, \xi\eta, \eta^2, \xi^3, \xi^2\eta, \xi\eta^2, \eta^3\right\}^{\mathrm{T}} & (q=3) \end{cases}. \tag{7}$$

The $\mathbf{a}(\boldsymbol{\xi})$ can be determined by minimizing the weighted L_2 norm,

$$J = \sum_{I=1}^{NM} \widehat{W}(\boldsymbol{\xi} - \boldsymbol{\xi}_I) \left[\mathbf{p}^{\mathrm{T}}(\boldsymbol{\xi}_I)\, \mathbf{a}(\boldsymbol{\xi}) - u_I\right]^2, \tag{8}$$

where NM is the number of nodes within the domain of node $\boldsymbol{\xi}$ for which the weight function $\widehat{W}(\boldsymbol{\xi} - \boldsymbol{\xi}_I)$ cannot equal zero, and u_I denotes the nodal parameter of u at $\boldsymbol{\xi} = \boldsymbol{\xi}_I$.

By substituting $\mathbf{a}(\boldsymbol{\xi})$ into Eq. (5), the meshfree approximation of the displacement can be expressed as follows:

$$u^h(\boldsymbol{\xi}) = \sum_{I=1}^{NM} \Psi_I(\boldsymbol{\xi})\, u_I(\boldsymbol{\xi}) = \boldsymbol{\Psi}(\boldsymbol{\xi})\, \mathbf{U}, \tag{9}$$

where the shape function $\Psi_I(\boldsymbol{\xi})$ is defined by

$$\boldsymbol{\Psi_I}(\boldsymbol{\xi}) = \sum_{J=1}^{m} \mathrm{p}_J(\boldsymbol{\xi}) \left(A^{-1}(\boldsymbol{\xi})\, B(\boldsymbol{\xi})\right)_{JI} = \mathbf{p}^{\mathrm{T}}(\boldsymbol{\xi}) \left(\mathbf{A}^{-1}\mathbf{B}\right)_I. \tag{10}$$

The weight function $\widehat{W}(\boldsymbol{\xi} - \boldsymbol{\xi}_I)$ in Eq. (8) influences the smoothness property of MLS shape functions. The quadratic splines weight function is given as follows:

$$\widehat{W}(\boldsymbol{\xi} - \boldsymbol{\xi}_I) = \begin{cases} 1 - 6r^2 + 8r^3 - 3r^4 & (r \le 1) \\ 0 & (r > 1) \end{cases}, \quad r = \frac{|\boldsymbol{\xi} - \boldsymbol{\xi}_I|}{d^I_{max}}, \quad d^I_{\max} = \lambda d_c, \tag{11}$$

where d^I_{max} is the support radius of the node $\boldsymbol{\xi}_I$, d_c denotes the average nodal spacing, and λ represents the dimensionless size of the support domain. The optimized λ was found to vary in a range of 2 to 4 by Liu et. al[51].

For reproducing the polynomial of complete order, the 2D consistency condition for the mesh-

free approximation is given as follows:

$$\sum_{I=1}^{NM} \Psi_I(\boldsymbol{\xi})\,\mathbf{p}(\boldsymbol{\xi}_I) = \mathbf{p}(\boldsymbol{\xi})\,. \tag{12}$$

3. Isogeometric-meshfree coupling approach

3.1. Reproducing points for isogeometric basis functions

Reproducing conditions can be conveniently derived from the tensor product of B-spline basis functions [45]:

$$\sum_{i=1}^{n}\sum_{j=1}^{m} N_{i,p}(\xi)\,M_{j,q}(\eta)\left(\xi_i^{[\alpha]}\right)^{\alpha}\left(\eta_j^{[\beta]}\right)^{\beta} = \xi^{\alpha}\eta^{\beta} \quad (\alpha+\beta\le l)\,, \tag{13}$$

where l represents the order of completeness in the 2D coupled approximation. By simplifying Eq. (13), the following expression can be obtained as follows [45]:

$$\sum_{I=1}^{NB} N_I^{pq}(\boldsymbol{\xi})\,\mathbf{p}\left(\xi_I^{[l]}\right) = \mathbf{p}(\boldsymbol{\xi})\,, \tag{14}$$

where $N_I^{pq}(\xi)$ equals $N_{i,p}(\xi)M_{j,q}(\eta)$; NB represents the number of basis functions. The reproducing point vectors $\mathbf{p}\left(\boldsymbol{\xi}_I^{[l]}\right)$ are given by [45]

$$\mathbf{p}\left(\boldsymbol{\xi}_I^{[l]}\right)^{\mathrm{T}} = \left\{1, \xi_I^{[1]}, \eta_I^{[1]}, \left(\xi_I^{[2]}\right)^2, \xi_I^{[1]}\eta_I^{[1]}, \left(\eta_I^{[2]}\right)^2, \cdots, \left(\xi_I^{[p]}\right)^p, \cdots, \left(\eta_I^{[q]}\right)^q\right\}\,. \tag{15}$$

3.2. IMF coupling approach

In the IGA-RKPM coupled approach, the reproducing kernel approximation and the MLS approximation are equivalent when monomial basis functions are applied. The NURBS basis functions and the MLS shape functions are coupled in the parametric domain. The parametric domain is constituted of two sub-domains: the IGA Ω^{IGA} and the meshfree Ω^{MF}. The coupling region between these two sub-domains is Ω^{CP}.

The displacement $u_{\mathrm{I}}(\mathbf{x})$ represented by the coupled approach can be defined as the linear combination of shape functions and nodal displacements:

$$u_I(\mathbf{x}) = \sum_{I=1}^{NS} \Phi_I(\boldsymbol{\xi})\,u_I, \tag{16}$$

where $\mathbf{x} = [x,y]^T$ represent space coordinates, NS is the number of shape functions, and u_I is the nodal displacement. $\Phi_I(\boldsymbol{\xi})$ is the value of shape function [45]

$$\Phi_I(\boldsymbol{\xi}) = \begin{cases} R_I(\boldsymbol{\xi}) & \boldsymbol{\xi}_I \in \Omega_{\xi}^{\mathrm{IGA}} \\ R_I(\boldsymbol{\xi}) + \Psi_I(\boldsymbol{\xi}) & \boldsymbol{\xi}_I \in \Omega_{\xi}^{\mathrm{CP}} \\ \Psi_I(\boldsymbol{\xi}) & \boldsymbol{\xi}_I \in \Omega_{\xi}^{\mathrm{MF}} \end{cases}, \tag{17}$$

where $\Psi_I(\boldsymbol{\xi})$ and $R_I(\boldsymbol{\xi})$ represent the MLS shape functions and the NURBS basis functions, respectively.

Based on the consistency conditions, the coupled basis functions can be obtained in a similar way to Eq. (12) and Eq. (14). In the coupling region, the reproducing condition is given as follows [45]:

$$\sum_{I=1}^{NS} \Phi_I(\boldsymbol{\xi})\, p\left(\boldsymbol{\xi}_I^{[l]}\right) = \sum_{J=1}^{NM} \Psi_J(\boldsymbol{\xi})\, \mathbf{p}\left(\boldsymbol{\xi}_J^{[l]}\right) + \sum_{I=1}^{NB} R_I(\boldsymbol{\xi})\, \mathbf{p}\left(\boldsymbol{\xi}_I^{[l]}\right) = \mathbf{p}(\boldsymbol{\xi}), \tag{18}$$

where NM and NB denote the number of the MLS shape functions and NURBS basis functions, respectively.

The MLS shape function in the coupling region can be expressed in the same way as the form of Eq. (10):

$$\Psi_J(\boldsymbol{\xi}) = \mathbf{p}^{\mathrm{T}}\left(\boldsymbol{\xi}_J^{[l]}\right) \mathbf{c}(\boldsymbol{\xi})\, \widehat{W}\left(\boldsymbol{\xi} - \boldsymbol{\xi}_J^{[1]}\right). \tag{19}$$

By substituting Eq. (19) into Eq. (18), $\mathbf{c}(\boldsymbol{\xi})$ can be obtained as follows:

$$\mathbf{c}(\boldsymbol{\xi}) = \mathbf{C}^{-1}(\boldsymbol{\xi})\left[\mathbf{p}(\boldsymbol{\xi}) - \mathbf{q}(\boldsymbol{\xi})\right], \tag{20}$$

$$\mathbf{C}(\boldsymbol{\xi}) = \sum_{J=1}^{NM} \mathbf{p}\left(\boldsymbol{\xi}_J^{[l]}\right) \mathbf{p}^T\left(\boldsymbol{\xi}_J^{[l]}\right) \widehat{W}\left(\boldsymbol{\xi} - \boldsymbol{\xi}_J^{[1]}\right), \tag{21}$$

$$\mathbf{q}(\boldsymbol{\xi}) = \sum_{I=1}^{NB} R_I(\boldsymbol{\xi})\, \mathbf{p}\left(\boldsymbol{\xi}_I^{[l]}\right). \tag{22}$$

Therefore, the modified MLS shape function in the coupling region can be finally represented as follows [45]:

$$\Psi_J(\boldsymbol{\xi}) = \mathbf{p}^T\left(\boldsymbol{\xi}_J^{[l]}\right) \mathbf{C}^{-1}(\boldsymbol{\xi})\left[\mathbf{p}(\boldsymbol{\xi}) - \mathbf{q}(\boldsymbol{\xi})\right] \widehat{W}\left(\boldsymbol{\xi} - \boldsymbol{\xi}_J^{[1]}\right). \tag{23}$$

Fig. 1 illustrates quadratic shape functions of the coupled approximation. It can be concluded that the smooth transition from isogeometric to meshfree approximation over the IGA subdomain, coupling region and meshfree sub-domain is implemented. The consistency conditions are achieved for the coupled approximation in the entire domain.

4. Thin-shell formulation

In thin-shell theory, the 3D continuum description is reduced to the shell mid-surface, and the transverse normal stress is neglected. Furthermore, the KL theory assumes that the shell cross-section remains normal to its mid-surface in the deformed configuration, which implies that the strain is assumed to be linear through the thickness and the transverse shear strains are zero.

4.1. Kinematics of the shell

The position of a material point in the reference configuration is described as follows:

$$\mathbf{X}_0\left(\xi^1, \xi^2, \xi^3\right) = \boldsymbol{\varphi}_0\left(\xi^1, \xi^2\right) + \xi^3 \mathbf{t}\left(\xi^1, \xi^2\right), \tag{24}$$

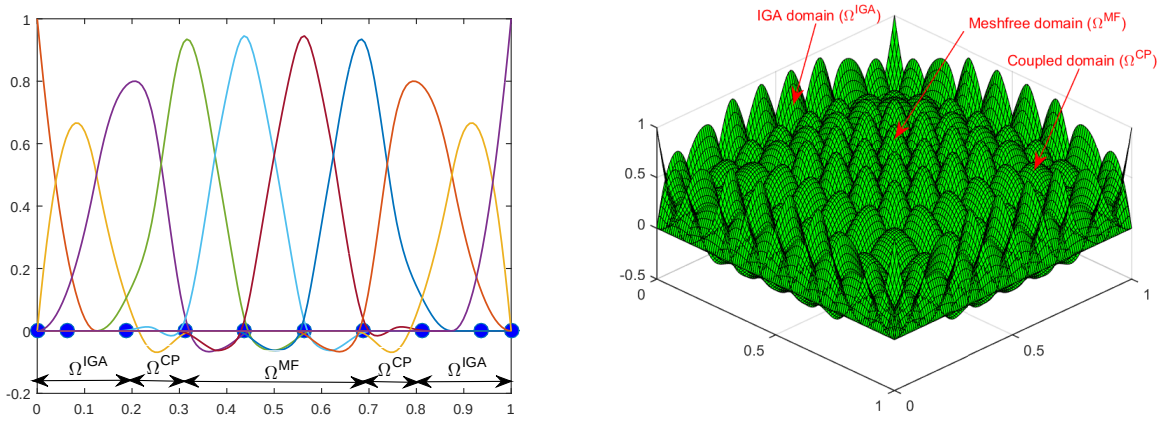

(a) (b)

Figure 1: (a) The IMF shape functions approximation with $p = 2$ in 1D, and (b) the IMF shape functions in 2D.

where $\xi^1, \xi^2 \in \mathbb{R}^2$ are convective curvilinear coordinates, $-0.5h \leq \xi^3 \leq 0.5h$ denotes the thickness of the material point, h is the thickness, $\mathbf{t}$ is the normal vector of the middle surface, and $\boldsymbol{\varphi}_0\left(\xi^1, \xi^2\right) : \mathbb{R}^2 \to \mathbb{R}^3$ is the position of a material point of the shell mid-surface in the reference configuration.

The covariant basis vectors are defined as follows:

$$\mathbf{G}_\alpha = \frac{\partial \mathbf{X}_0}{\partial \xi^\alpha} = \boldsymbol{\varphi}_{0,\alpha} + \xi^3 \frac{\partial \mathbf{t}_\alpha}{\partial \xi^\alpha} \;\; ; \qquad \mathbf{G}_3 = \frac{\partial \mathbf{X}_0}{\partial \xi^3} = \mathbf{t} \qquad (\alpha = 1,2) \tag{25}$$

The mid-surface unit normal vectors in the reference configuration and deformed configuration are calculated as follows:

$$\mathbf{G}_3 = \frac{\mathbf{G}_1 \times \mathbf{G}_2}{|\mathbf{G}_1 \times \mathbf{G}_2|} \;\; , \quad \mathbf{g}_3 = \frac{\mathbf{g}_1 \times \mathbf{g}_2}{|\mathbf{g}_1 \times \mathbf{g}_2|}. \tag{26}$$

The covariant metric coefficients of the surface are defined as

$$G_{ij} = \mathbf{G}_i \cdot \mathbf{G}_j \;\; , \quad g_{ij} = \mathbf{g}_i \cdot \mathbf{g}_j \qquad (i,j = 1,2,3) \;\; , \tag{27}$$

and the contravariant basis vectors are computed by

$$\mathbf{G}^i = G^{ij}\mathbf{G}_j \;\; , \quad G^{ij} = \left\{G_{ij}\right\}^{-1} . \tag{28}$$

The Green-Lagrange strain tensor is expressed as follows:

$$\mathbf{E} = E_{ij}\mathbf{G}^i \otimes \mathbf{G}^j \;\; , \quad E_{ij} = \frac{1}{2}\left(g_{ij} - G_{ij}\right). \tag{29}$$

The Green-Lagrange strain is decomposed into a constant part due to membrane action and a linear

part due to bending. The in-plane strain coefficients are given by

$$\mathbf{E} = E_{\alpha\beta}\mathbf{G}^{\alpha} \otimes \mathbf{G}^{\beta} \ . \tag{30}$$

Substituting metric coefficients given in Eq. (27) into Eq. (30), in-plane strain coefficients reduce to

$$E_{\alpha\beta} = \varepsilon_{\alpha\beta} + \xi^3 \kappa_{\alpha\beta}, \tag{31}$$

The membrane strains $\varepsilon_{\alpha\beta}$ are given by

$$\varepsilon_{\alpha\beta} = \frac{1}{2}\left(\mathbf{g}_{\alpha} \cdot \mathbf{g}_{\beta} - \mathbf{G}_{\alpha} \cdot \mathbf{G}_{\beta}\right), \tag{32}$$

and the bending strains $\kappa_{\alpha\beta}$ are given by

$$\kappa_{\alpha\beta} = \mathbf{G}_{\alpha,\beta} \cdot \mathbf{G}_3 - \mathbf{g}_{\alpha,\beta} \cdot \mathbf{g}_3. \tag{33}$$

4.2. Weak form

Applying the principle of virtual work, we obtain the stationarity of the total potential

$$\delta W = \delta W_{\text{int}} + \delta W_{\text{ext}} = 0. \tag{34}$$

The internal virtual work δW_{int} is described as follows:

$$\delta W_{\text{int}} = -\int_{\Omega_0} \delta\mathbf{E} : \mathbf{S} \mathrm{d}\Omega_0, \tag{35}$$

The second Piola-Kirchhoff stress is given as follows:

$$S^{\alpha\beta} = C^{\alpha\beta\gamma\delta} E_{\gamma\delta}, \tag{36}$$

with

$$C^{\alpha\beta\gamma\delta} = \frac{E}{1-\nu^2}\left[\nu A^{\alpha\beta}A^{\gamma\delta} + \frac{1}{2}(1-\nu)\left(A^{\alpha\gamma}A^{\delta\beta} + A^{\alpha\delta}A^{\gamma\beta}\right)\right], \tag{37}$$

where E is the Young's modulus, ν is the Poisson's ratio and $A^{\alpha\beta}$ are contravariant metric coefficients. The external virtual work δW_{ext} is calculated as follows:

$$\delta W_{\text{ext}} = \int_{\Omega_0} \mathbf{b} \cdot \delta\mathbf{u} d\Omega_0 + \int_{\Gamma_0} \bar{\mathbf{t}}_0 \cdot \delta\mathbf{u} \mathrm{d}\Gamma_0, \tag{38}$$

where $\mathbf{b}$ is the body force per unit area and $\bar{\mathbf{t}}_0$ is the prescribed traction per unit length in the reference configuration.

Substituting Eq. (31) and Eq. (36) into Eq. (35) yields [52]

$$\delta W_{\text{int}} = -\int_{\Omega_0} \delta\mathbf{E} : \mathbf{S} \mathrm{d}\Omega_0 = -\int_{\Omega_0} \left(\delta\varepsilon_{\alpha\beta} + \xi^3 \delta\kappa_{\alpha\beta}\right) \mathrm{C}^{\alpha\beta\gamma\delta} \left(\varepsilon_{\gamma\delta} + \xi^3 \kappa_{\gamma\delta}\right) \mathrm{d}\Omega_0, \tag{39}$$

Integrating Eq. (39) through the thickness gives to the Koiter's nonlinear shell model:

$$\begin{aligned} -\int_{\Omega_0} \delta\mathbf{E} : \mathbf{S}\mathrm{d}\Omega_0 &= -\int_{\Omega} \left(h\delta\varepsilon_{\alpha\beta}\mathrm{C}^{\alpha\beta\gamma\delta}\varepsilon_{\gamma\delta} + \frac{h^3}{12}\delta\kappa_{\alpha\beta}\mathrm{C}^{\alpha\beta\gamma\delta}\kappa_{\gamma\delta} \right)\mathrm{d}\Omega \\ &= -\int_{\Omega} \left(\mathrm{n}^{\alpha\beta}\delta\varepsilon_{\alpha\beta} + \mathrm{m}^{\alpha\beta}\delta\kappa_{\alpha\beta} \right)\mathrm{d}\Omega \end{aligned} \tag{40}$$

where $\mathrm{n}^{\alpha\beta}$ and $\mathrm{m}^{\alpha\beta}$ are the membrane stress and the bending components, respectively. For the elastic isotropic material, these stress can be described using the Voigt's notation:

$$\mathbf{n} = \begin{bmatrix} n^{11} \\ n^{22} \\ n^{12} \end{bmatrix} = h\mathbf{C} \begin{bmatrix} \varepsilon_{11} \\ \varepsilon_{22} \\ 2\varepsilon_{12} \end{bmatrix} = h\mathbf{C}\boldsymbol{\varepsilon}, \tag{41}$$

$$\mathbf{m} = \begin{bmatrix} m^{11} \\ m^{22} \\ m^{12} \end{bmatrix} = \frac{h^3}{12}\mathbf{C} \begin{bmatrix} \kappa_{11} \\ \kappa_{22} \\ 2\kappa_{12} \end{bmatrix} = \frac{h^3}{12}\mathbf{C}\boldsymbol{\kappa}. \tag{42}$$

with

$$\mathbf{C} = \frac{E}{1-\nu^2} \begin{bmatrix} (A_{11})^2 & \nu A_{11}A_{22} + (1-\nu)(A_{12})^2 & A_{11}A_{12} \\ \vdots & (A_{22})^2 & A_{22}A_{12} \\ sym. & \cdots & \frac{1}{2}\left[(1-\nu)A_{11}A_{22} + (1+\nu)(A_{12})^2\right] \end{bmatrix}. \tag{43}$$

The following internal virtual work is integrated through the thickness [53],

$$-\int_{\Omega_0} \delta\mathbf{E} : \mathbf{S}\mathrm{d}\Omega_0 = -\int_{A} (\mathbf{n} : \delta\boldsymbol{\varepsilon} + \mathbf{m} : \delta\boldsymbol{\kappa})\mathrm{d}A, \tag{44}$$

where $\mathrm{d}A$ is the differential area of the middle surface in the reference configuration given as follows:

$$\mathrm{d}A = \bar{j}_0 d\xi^1 d\xi^2. \tag{45}$$

with the determinant $\bar{j}_0 = \|\mathbf{A}_1 \times \mathbf{A}_2\|$ of the Jacobian of the middle surface in the reference configuration.

The first derivative of δW_{int} yields the residual force vector $\mathbf{R}$:

$$R_r = \left(\frac{\partial W_{\mathrm{int}}}{\partial u_r} + \frac{\partial W_{\mathrm{ext}}}{\partial u_r} \right) = F_r^{\mathrm{int}} + F_r^{\mathrm{ext}}, \tag{46}$$

where F_r^{ext} is the external force and F_r^{int} is the internal force given as below,

$$F_r^{\mathrm{int}} = -\int_{A} \left(\mathbf{n} : \frac{\partial\boldsymbol{\varepsilon}}{\partial u_r} + \mathbf{m} : \frac{\partial\boldsymbol{\kappa}}{\partial u_r} \right)\mathrm{d}A. \tag{47}$$

The second derivative of the virtual work gives to the stiffness matrix, including the internal

part and external part:

$$K_{rs} = -\left(\frac{\partial^2 W_{\text{int}}}{\partial u_r \partial u_s} + \frac{\partial^2 W_{\text{ext}}}{\partial u_r \partial u_s}\right) = K_{rs}^{\text{int}} + K_{rs}^{\text{ext}}, \tag{48}$$

where K_{rs}^{int} is the internal stiffness matrix and K_{rs}^{ext} is the derivative of the external load w.r.t. displacements. The internal stiffness K_{rs}^{int} including the membrane part and bending part, is computed as follows,

$$K_{rs}^{\text{int}} = \int_A \left(\frac{\partial \mathbf{n}}{\partial u_s} : \frac{\partial \boldsymbol{\varepsilon}}{\partial u_r} + \frac{\partial \mathbf{m}}{\partial u_s} : \frac{\partial \boldsymbol{\kappa}}{\partial u_r}\right) \mathrm{d}A. \tag{49}$$

5. Extended isogeometric-meshfree coupling approach (XIMF)

5.1. Discretization of the displacement field

The main concept underlying XFEM is to achieve the extension of the approximation basis by a set of enrichment functions selected for presenting the local behaviors in the problem domain. Similar to the enrichment strategy used in XFEM, the XIMF displacement field of the cracked shell surface can be expressed as

$$\begin{aligned}\left\{\begin{array}{c} u_1 \\ u_2 \end{array}\right\} = &\sum_{I=1}^{NS} \Phi_I(x_I) \left\{\begin{array}{c} u_{I1} \\ u_{I2} \end{array}\right\} + \sum_{J=1}^{NH} \Phi_J(\xi)\left[H(\xi) - H(\xi_J)\right] \left\{\begin{array}{c} a_{J1} \\ a_{J2} \end{array}\right\} \\ &+ \sum_{K=1}^{NT} \Phi_K(\xi) \left\{\sum_{\alpha=1}^{4} \left[Q_\alpha(\xi) - Q_\alpha(\xi_K)\right] \left\{\begin{array}{c} b_{K1}^\alpha \\ b_{K2}^\alpha \end{array}\right\}\right\},\end{aligned} \tag{50}$$

$$u_3 = \sum_{I=1}^{NS} \Phi_I(x_I)\, u_{I3} + \sum_{J=1}^{NH} \Phi_J(\xi)\left[H(\xi) - H(\xi_J)\right] a_{J3} + \sum_{K=1}^{NT} \Phi_K(\xi) \left\{\sum_{\alpha=1}^{4} \left[F_\alpha(\xi) - F_\alpha(\xi_K)\right] b_{K3}^\alpha\right\}, \tag{51}$$

where Φ_I represent the IMF basis functions; u_1, u_2, u_3 are the standard DOFs; a_1, a_2, a_3 are the DOFs associated with the crack face; b_1, b_2, b_3 are the additional DOFs at the crack tip; H are the Heaviside functions; Q and F are the in-plane and out-of-plane tip-enrichment functions, respectively. Fig. 2 illustrates the 1D step-enriched shape functions and the shape functions for $N_{5,2}$ in 2D domain. The in-plane tip enrichment function is given [54]

$$Q(r,\theta) = \left\{\sqrt{r}\sin\left(\frac{\theta}{2}\right), \sqrt{r}\cos\left(\frac{\theta}{2}\right), \sqrt{r}\sin\left(\frac{\theta}{2}\right)\sin(\theta), \sqrt{r}\cos\left(\frac{\theta}{2}\right)\sin(\theta)\right\}. \tag{52}$$

The corresponding out-of-plane tip enrichment function is given by [55]

$$F(r,\theta) = \left\{\sqrt{r}\sin\left(\frac{\theta}{2}\right), r^{\frac{3}{2}}\sin\left(\frac{\theta}{2}\right), r^{\frac{3}{2}}\cos\left(\frac{\theta}{2}\right), r^{\frac{3}{2}}\sin\left(\frac{3\theta}{2}\right), r^{\frac{3}{2}}\cos\left(\frac{3\theta}{2}\right)\right\}. \tag{53}$$

5.2. Domain form for J-integral calculation

Two states of a cracked model are chosen as the asymptotic fields for mode I and mode II: the present state $\left(\sigma_{ij}^{(1)}, \varepsilon_{ij}^{(1)}, u_i^{(1)}\right)$ and an auxiliary state $\left(\sigma_{ij}^{(2)}, \varepsilon_{ij}^{(2)}, u_i^{(2)}\right)$, respectively. Details about the asymptotic fields are given in the Appendix B.

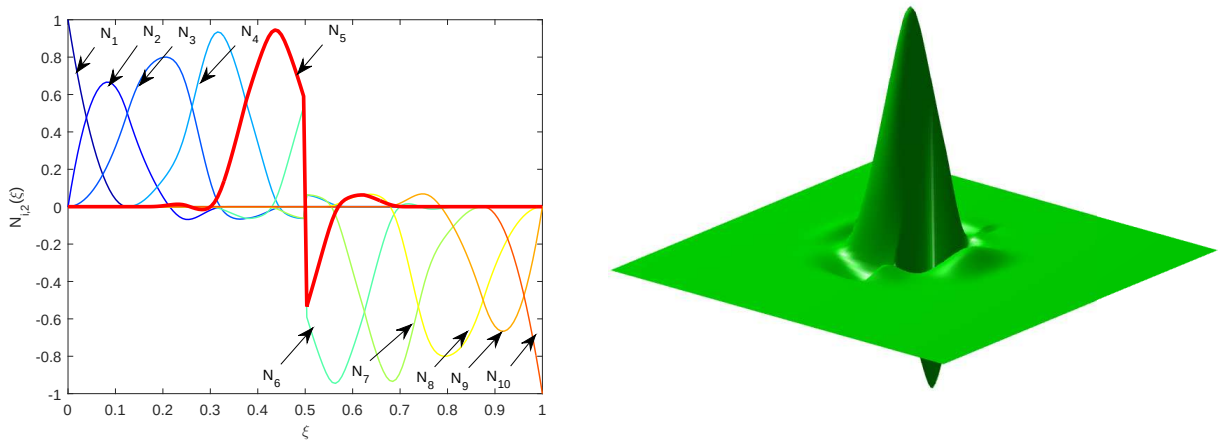

(a) (b)

Figure 2: (a) 1D Quadratic IMF coupled basis functions, and (b) step-enriched basis function with $N_{5,2}$ in 2D.

The J-integral for the sum of these two states is given as follows:

$$J^{(1+2)} = \int_{\Gamma} \left[\frac{1}{2} \left(\sigma_{ij}^{(1)} + \sigma_{ij}^{(2)} \right) \left(\varepsilon_{ij}^{(1)} + \varepsilon_{ij}^{(2)} \right) \delta_{1j} - \left(\sigma_{ij}^{(1)} + \sigma_{ij}^{(2)} \right) \frac{\partial \left(u_i^{(1)} + u_i^{(2)} \right)}{\partial x_1} \right] n_j d\Gamma \,, \quad (54)$$

where σ_{ij} are the stress tensor components, ε_{ij} are the strain tensor components, n_j are the components of the unit normal vector to Γ, u_i are the displacement components, and δ_{1j} is the Kronecker delta.

By expanding and rearranging the terms in Eq. (54), the following equation can be given as follows:

$$J^{(1+2)} = J^{(1)} + J^{(2)} + I^{(1,2)} \,, \quad (55)$$

where $J^{(1)}$ is the J-integral for the present state and $J^{(2)}$ is the integral for the auxiliary state. The interaction integral $I^{(1,2)}$ is defined as follows:

$$I^{(1,2)} = \int_{A} \left[\sigma_{ij}^{(1)} \frac{\partial u_i^{(2)}}{\partial x_1} + \sigma_{ij}^{(2)} \frac{\partial u_i^{(1)}}{\partial x_1} - W^{(1,2)} \delta_{1,j} \right] \frac{\partial q}{\partial x_j} dA \,, \quad (56)$$

where A is the area inside the contour of integral, q is a smooth function varying from $q = 1$ on the interior boundary of surface A to $q = 0$ on the outer one, and the interaction strain energy W is given as follows:

$$W^{(1,2)} = \frac{1}{2} \left(\sigma_{ij}^{(1)} \varepsilon_{ij}^{(2)} + \sigma_{ij}^{(2)} \varepsilon_{ij}^{(1)} \right) \,. \quad (57)$$

A through-the-thickness crack with the crack front normal to the mid-surface of the shell model

is considered. The J-integral is defined as [56]

$$fJ = \int_A \left(\sigma_{ij} \frac{\partial u_i}{\partial x_1} - W \delta_{1j} \right) n_j \bar{q} dA \ . \tag{58}$$

Applying the divergence theorem to Eq. (58), we obtain

$$fJ = \int_V \left(\sigma_{ij} \frac{\partial u_i}{\partial x_1} - W \delta_{1j} \right) \frac{\partial \bar{q}}{\partial x_j} dV - \int_{A_1+A_2} \left(\sigma_{ij} \frac{\partial u_i}{\partial x_1} - W \delta_{1j} \right) n_j \bar{q} dA \ . \tag{59}$$

The cylindrical shell around the crack front is limited by the upper and lower faces A_1 and A_2, respectively. Assuming that A_1 and A_2 are equal and orthogonal to the crack front, we have

$$\begin{array}{l} n_1 = n_2 = 0 \ , \ n_3 = 1 \quad \text{on} \ \ A_1 \\ n_1 = n_2 = 0 \ , \ n_3 = -1 \quad \text{on} \ \ A_2 \end{array} \ .$$

The $\bar{q}$ function is taken to be constant through the shell thickness; $f = h$ and is equal to 1 on A_ε. Eq. (59) can be rewritten as

$$hJ = \int_V \left(\sigma_{ij} \frac{\partial u_i}{\partial x_1} - \frac{1}{2} \sigma_{ij} \varepsilon_{ij} \delta_{1j} \right) \frac{\partial \bar{q}}{\partial x_j} dV - \int_{A_1+A_2} \sigma_{i3} \frac{\partial u_i}{\partial x_1} n_3 \bar{q} dA \ . \tag{60}$$

The domain form of the J-integral of the two states is given as follows:

$$\begin{aligned} J^{(1+2)} = & \frac{1}{h} \int_V \left(\left(\sigma_{ij}^1 + \sigma_{ij}^2 \right) \frac{\partial \left(u_i^1 + u_i^2 \right)}{\partial x_1} - \frac{1}{2} \left(\sigma_{ij}^1 + \sigma_{ij}^2 \right) \left(\varepsilon_{ij}^1 + \varepsilon_{ij}^2 \right) \delta_{1j} \right) \frac{\partial \bar{q}}{\partial x_j} dV \\ & - \frac{1}{h} \int_{A_1+A_2} \left(\sigma_{i3}^1 + \sigma_{i3}^2 \right) \frac{\partial \left(u_i^1 + u_i^2 \right)}{\partial x_1} n_3 \bar{q} dA \end{aligned} \ . \tag{61}$$

Eq. (61) can be written as

$$J^{(1+2)} = J^{(1)} + J^{(2)} + I^{(1,2)} \ , \tag{62}$$

where

$$J^{(a)} = \frac{1}{h} \int_V \left(\sigma_{ij}^a \frac{\partial u_i^a}{\partial x_1} - \frac{1}{2} \sigma_{ij}^a \varepsilon_{ij}^a \delta_{1j} \right) \frac{\partial \bar{q}}{\partial x_j} dV - \frac{1}{h} \int_{A_1+A_2} \sigma_{i3}^a \frac{\partial u_i^a}{\partial x_1} n_3 \bar{q} dA \ , \tag{63}$$

and the interaction integral is given as follows:

$$I^{(1,2)} = \frac{1}{h} \int_V \left(\sigma_{ij}^1 \frac{\partial u_i^2}{\partial x_1} + \sigma_{ij}^2 \frac{\partial u_i^1}{\partial x_1} - \sigma_{ij}^1 \varepsilon_{ij}^2 \delta_{1j} \right) \frac{\partial \bar{q}}{\partial x_j} dV - \frac{1}{h} \int_{A_1+A_2} \left(\sigma_{ij}^1 \frac{\partial u_i^2}{\partial x_1} + \sigma_{ij}^2 \frac{\partial u_i^1}{\partial x_1} \right) n_3 \bar{q} dA \ . \tag{64}$$

The relationship between the interaction integral and the SIFs is given as follows:

$$I^{(1,2)} = \frac{2}{E} \left(K_I^1 K_I^2 + K_{II}^1 K_{II}^2 \right) + \frac{2\pi}{3E} \left(\frac{1+\nu}{3+\nu} \right) \left(k_1^1 k_1^2 + k_2^1 k_2^2 \right) \ . \tag{65}$$

The J-integral is given as follows:

$$J^{(1+2)} = J^{(1)} + J^{(2)} + \frac{2}{E}\left(K_I^1 K_I^2 + K_{II}^1 K_{II}^2\right) + \frac{2\pi}{3E}\left(\frac{1+\nu}{3+\nu}\right)\left(k_1^1 k_1^2 + k_2^1 k_2^2\right) \ , \tag{66}$$

where K_I and K_{II} are the SIFs associated with the symmetric and antisymmetric membrane loading, respectively.

$$K_I = \lim_{r\to 0}\sqrt{2\pi r}\sigma_{\theta\theta}\left(r,\theta\right) \ \ ; \qquad K_{II} = \lim_{r\to 0}\sqrt{2\pi r}\sigma_{r\theta}\left(r,\theta\right) \ ,$$

and k_1 and k_2 are the bending and twisting loadings:

$$k_1 = \lim_{r\to 0}\sqrt{2r}\sigma_{\theta\theta}\left(r,0,\frac{h}{2}\right) \ \ ; \qquad k_2 = \lim_{r\to 0}\frac{3+\nu}{1+\nu}\sqrt{2r}\sigma_{r\theta}\left(r,0,\frac{h}{2}\right) \ .$$

5.3. Discretization of fracture in thin shells

The deformed and undeformed shell middle surfaces can be defined in terms of basis function $\Phi_I(\xi)$,

$$\varphi\left(\xi^1,\xi^2\right) = \sum_{I=1}^{NS}\Phi_I\left(\boldsymbol{\xi}\right)p_I^* \ , \quad \varphi_0\left(\xi^1,\xi^2\right) \ = \sum_{I=1}^{NS}\Phi_I\left(\boldsymbol{\xi}\right)p_I, \tag{67}$$

where $p_I, p_I^* \in \mathbb{R}^3$ are control points in the initial and deformed configurations, respectively.
The membrane and bending strains can be expressed in Voigt notation, shown as follows [57],

$$\boldsymbol{\varepsilon} = \begin{bmatrix} \varepsilon_{11} \\ \varepsilon_{22} \\ 2\varepsilon_{12} \end{bmatrix} = \sum_{I=1}^{NS}\mathbf{B}_{\mathrm{m}}^I u_I \ , \quad \boldsymbol{\kappa} = \begin{bmatrix} \kappa_{11} \\ \kappa_{22} \\ 2\kappa_{12} \end{bmatrix} = \sum_{I=1}^{NS}\mathbf{B}_{\mathrm{b}}^I u_I, \tag{68}$$

where the membrane matrix $\mathbf{B}_{\mathrm{m}}^I$ and the bending matrix $\mathbf{B}_{\mathrm{b}}^I$ are expressed as follows:

$$\mathbf{B}_{\mathrm{m}}^I = \begin{bmatrix} \left(\mathbf{A}_1\Phi_{I,1}\right)^T \\ \left(\mathbf{A}_2\Phi_{I,2}\right)^T \\ \left(\mathbf{A}_1\Phi_{I,2} + \mathbf{A}_2\Phi_{I,1}\right)^T \end{bmatrix} \ , \quad \mathbf{B}_{\mathrm{b}}^I = \begin{bmatrix} \left(\mathbf{b}_{\mathrm{b}11}^I\right)^T \\ \left(\mathbf{b}_{\mathrm{b}22}^I\right)^T \\ \left(2\mathbf{b}_{\mathrm{b}12}^I\right)^T \end{bmatrix} \ , \tag{69}$$

with

$$\begin{aligned} \mathbf{b}_{\mathrm{b}\alpha\beta}^I =& \mathbf{A}_{\alpha,\beta}\cdot\mathbf{A}_3\frac{1}{\bar{j}_0}\left[\Phi_{I,1}\left(\mathbf{A}_2\times\mathbf{A}_3\right) + \Phi_{I,2}\left(\mathbf{A}_3\times\mathbf{A}_1\right)\right] \\ & - \frac{1}{\bar{j}_0}\left[\Phi_{I,1}\left(\mathbf{A}_2\times\mathbf{A}_{\alpha,\beta}\right) + \Phi_{I,2}\left(\mathbf{A}_{\alpha,\beta}\times\mathbf{A}_1\right)\right] - \Phi_{I,\alpha\beta}\mathbf{A}_3 \end{aligned} \ . \tag{70}$$

The $\mathbf{B}_{\mathscr{H}}^{\mathrm{m}}$ associated to the Heaviside enrichment is given as follows:

$$\mathbf{B}_{\mathscr{H}}^{\mathrm{m}J} = \begin{bmatrix} \left[\mathbf{A_1}\left(H\left(\xi\right) - H\left(\xi_J\right)\right)\Phi_{J,1}\right]^T \\ \left[\mathbf{A_2}\left(H\left(\xi\right) - H\left(\xi^J\right)\right)\Phi_{J,2}\right]^T \\ \left[\left(\mathbf{A_2}\Phi_{J,1} + \mathbf{A_1}\Phi_{J,2}\right)\left(H\left(\xi\right) - H\left(\xi_J\right)\right)\right]^T \end{bmatrix} \ . \tag{71}$$

The $\mathbf{B}^{\mathrm{m}}_{\mathscr{T}}$ associated to the tip enrichment is

$$\mathbf{B}^{\mathrm{m}K}_{\mathscr{T}} = \begin{bmatrix} \left[\left\{\Phi_{K,1}\left(\Psi_K\left(\xi\right)-\Psi_K\left(\xi_K\right)\right)+\Phi_K Q_{K,1}\left(\xi\right)\right\}\mathbf{A_1}\right]^T \\ \left[\left\{\Phi_{K,2}\left(Q_K\left(\xi\right)-Q_K\left(\xi_K\right)\right)+\Phi_K \Psi_{K,2}\left(\xi\right)\right\}\mathbf{A_2}\right]^T \\ \left[\left(\mathbf{A_2}\Phi_{K,1}+\mathbf{A_1}\Phi_{K,2}\right)\left(Q_K\left(\xi\right)-Q_K\left(\xi_K\right)\right)+\Phi_K\left(\Phi_K Q_{K,1}\left(\xi\right)\mathbf{A_2}+\Phi_K Q_{K,1}\left(\xi\right)\mathbf{A_1}\right)\right]^T \end{bmatrix}. \tag{72}$$

The $\mathbf{B}^{\mathrm{b}J}_{\mathscr{H}}$-matrix associated with the Heaviside-enriched DOFs is given as follows:

$$\mathbf{B}^{\mathrm{b}J}_{\mathscr{H}} = \left(H\left(\xi\right)-H\left(\xi_J\right)\right)\begin{bmatrix} \left(\mathbf{b}^{bJ}_{\mathscr{H}_{11}}\right)^T \\ \left(\mathbf{b}^{bJ}_{\mathscr{H}_{22}}\right)^T \\ \left(2\mathbf{b}^{bJ}_{\mathscr{H}_{12}}\right)^T \end{bmatrix}, \tag{73}$$

where $\mathbf{b}^{\mathbf{bJ}}_{\mathscr{H}_{\mathbf{11}}}, \mathbf{b}^{\mathbf{bJ}}_{\mathscr{H}_{\mathbf{22}}}, \mathbf{b}^{\mathbf{bJ}}_{\mathscr{H}_{\mathbf{12}}}$ are the same as the standard membrane terms. The contribution of the crack tip enrichment is calculated by

$$\mathbf{B}^{bK}_{\mathscr{T}} = \begin{bmatrix} \left(\mathbf{b}^{bK}_{\mathscr{T}_{11}}\right)^T \\ \left(\mathbf{b}^{bK}_{\mathscr{T}_{22}}\right)^T \\ \left(2\mathbf{b}^{bK}_{\mathscr{T}_{12}}\right)^T \end{bmatrix}, \tag{74}$$

where $\mathbf{b}^{\mathbf{bJ}}_{\mathscr{T}_{\mathbf{11}}}, \mathbf{b}^{\mathbf{bJ}}_{\mathscr{T}_{\mathbf{22}}}, \mathbf{b}^{\mathbf{bJ}}_{\mathscr{T}_{\mathbf{12}}}$ are similar to the standard bending terms, but replacing $\Phi_{I1}, \Phi_{I2}, \Phi_{I12}, \Phi_{I11}, \Phi_{I22}$ by the following terms:

$$\begin{aligned} \Phi_{I,11} &= \Phi_{K,11}\left(Q_K\left(\xi\right)-Q_K\left(\xi_K\right)\right)+2\Phi_{I,1}Q_{K,1}\left(\xi\right)+\Phi_I Q_{K,11}\left(\xi\right) \\ \Phi_{I,22} &= \Phi_{K,22}\left(Q_K\left(\xi\right)-Q_K\left(\xi_K\right)\right)+2\Phi_{I,2}Q_{K,2}\left(\xi\right)+\Phi_I Q_{K,22}\left(\xi\right) \\ \Phi_{I,12} &= \Phi_{K,12}\left(Q_K\left(\xi\right)-Q_K\left(\xi_K\right)\right)+\Phi_{I,1}Q_{K,2}\left(\xi\right)+\Phi_{I,2}Q_{K,1}\left(\xi\right)+\Phi_I Q_{K,12}\left(\xi\right). \\ \Phi_{I,1} &= \Phi_{K,1}\left(Q_K\left(\xi\right)-Q_K\left(\xi_K\right)\right)+\Phi_I Q_{K,1}\left(\xi\right) \\ \Phi_{I,2} &= \Phi_{K,2}\left(Q_K\left(\xi\right)-Q_K\left(\xi_K\right)\right)+\Phi_I Q_{K,2}\left(\xi\right) \end{aligned} \tag{75}$$

The first derivative of Eq. (67) w.r.t. the nodal displacement yields,

$$\frac{\partial \boldsymbol{\varphi}}{\partial u_r} = \sum_{I=1}^{NS} \Phi_I\left(\xi\right)\left(p_I+u_I\right)_{,r} = \sum_{I=1}^{NS} \Phi_I\left(\xi\right) u_{I,r}, \tag{76}$$

and the first derivative of covariant basis vectors is calculated as follows:

$$\frac{\partial \mathbf{a}_\alpha}{\partial u_r} = \frac{\partial}{\partial u_r}\left(\frac{\partial \boldsymbol{\varphi}}{\partial \xi^\alpha}\right) = \sum_{I=1}^{NS} \Phi_{I,\alpha}\left(\xi\right) u_{I,r}. \tag{77}$$

The first and second derivatives of strains and stresses w.r.t. nodal displacements can be obtained. The details are presented in Appendix A.

Substituting $\boldsymbol{\varepsilon}$, $\boldsymbol{\kappa}$, $\mathbf{n}$, $\mathbf{m}$ and derivatives into Eq. (49) gives global stiffness matrices of the linear

part. Therefore, linearized systems are given as follows:

$$\mathbf{Ku} = \mathbf{F}. \tag{78}$$

The dynamical discrete equation can be obtained as

$$\mathbf{M\ddot{u}} + \mathbf{Ku} = \mathbf{F}\ , \tag{79}$$

where $\mathbf{K}$ and $\mathbf{M}$ are the global stiffness and global mass matrices, respectively. The stiffness matrix can be expressed as follows:

$$\mathbf{K} = \begin{bmatrix} \mathrm{K}_{II} & \mathrm{K}_{IJ} \\ \mathrm{K}_{JI} & \mathrm{K}_{JJ} \end{bmatrix}\ , \tag{80}$$

where

$$\begin{aligned}
\mathrm{K}_{II} &= \int_A \left(\mathbf{B}^I_{\mathrm{m}}\right)^T \mathbf{C}\mathbf{B}^I_{\mathrm{m}} dA + \int_A \left(\mathbf{B}^I_{\mathrm{b}}\right)^T \mathbf{C}\mathbf{B}^I_{\mathrm{b}} dA \\
\mathrm{K}_{IJ} &= \int_A \left(\mathbf{B}^{\mathrm{m}I}_{\mathscr{H}}\right)^T \mathbf{C}\mathbf{B}^{\mathrm{m}J}_{\mathscr{H}} dA + \int_A \left(\mathbf{B}^{\mathrm{b}I}_{\mathscr{H}}\right)^T \mathbf{C}\mathbf{B}^{\mathrm{b}J}_{\mathscr{H}} dA \\
\mathrm{K}_{JI} &= \int_A \left(\mathbf{B}^{\mathrm{m}J}_{\mathscr{H}}\right)^T \mathbf{C}\mathbf{B}^{\mathrm{m}I}_{\mathscr{H}} dA + \int_A \left(\mathbf{B}^{\mathrm{b}J}_{\mathscr{H}}\right)^T \mathbf{C}\mathbf{B}^{\mathrm{b}I}_{\mathscr{H}} dA \\
\mathrm{K}_{JJ} &= \int_A \left(\mathbf{B}^{\mathrm{m}J}_{\mathscr{T}}\right)^T \mathbf{C}\mathbf{B}^{\mathrm{m}J}_{\mathscr{T}} dA + \int_A \left(\mathbf{B}^{\mathrm{b}J}_{\mathscr{T}}\right)^T \mathbf{C}\mathbf{B}^{\mathrm{b}J}_{\mathscr{T}} dA\ .
\end{aligned} \tag{81}$$

The mass matrix is given by

$$\mathbf{M} = \begin{bmatrix} \mathrm{M}_{II} & \mathrm{M}_{IJ} \\ \mathrm{M}_{JI} & \mathrm{M}_{JJ} \end{bmatrix} = \begin{bmatrix} \int_A \Phi_I \rho \Phi_I h dA & \int_A \Phi_I \rho H \Phi_J h dA \\ \int_A H\Phi_J \rho \Phi_I h dA & \int_A H\Phi_J \rho H \Phi_J h dA \end{bmatrix}\ . \tag{82}$$

The free vibration can be expressed as follows:

$$\left(\mathbf{K} - \omega^2 \mathbf{M}\right)\delta = 0\ , \tag{83}$$

where ω is the natural frequency, δ is the eigenvector, h is the thickness, and ρ is the density mass.

6. Numerical problems

In this section, static and free vibration analyses of cracks for thin-shell structures are presented. The performance of the proposed approach is compared to the reference solutions. The weight function is the quartic spline with support sizes 2.5 for the quadratic shape function. For numerical integration, an 8×8 Gauss quadrature is used in the local refined region while 4×4 Gauss quadrature is employed in the rest region.

6.1. Static analysis

6.1.1. Infinite plate with a center crack under remote uniform tension

By considering an isotropic infinite plate with a central crack under remote uniform tension (Fig. 3), a unit square domain ABCD with an edge crack of length $2a = 10$ mm is modeled under

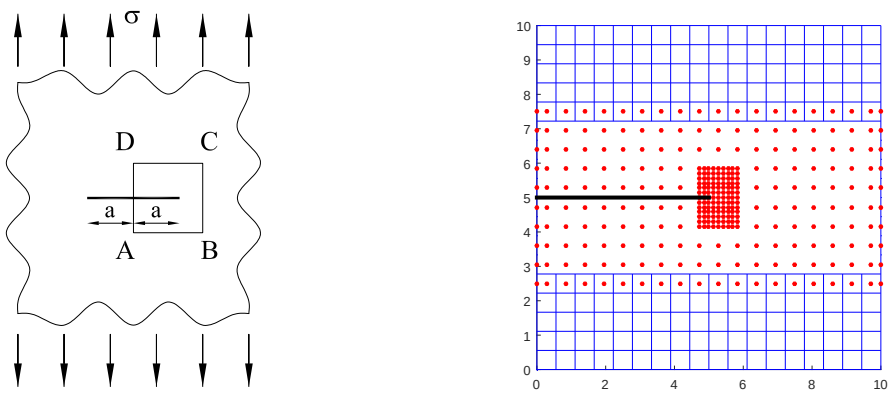

Figure 3: Infinite plate with a center crack under uniform tension loading and the local refinement mesh.

a plain-strain condition. The material properties are set as follows: $E = 10^7$ N/mm^2, $\nu = 0.3$, and $\sigma = 10^4$ N/mm^2. The exact solution for this problem is given as follows [58]:

$$\begin{cases} u_x(r,\theta) = \dfrac{2(1+\nu)}{\sqrt{2\pi}}\dfrac{K_{\mathrm{I}}}{E}\sqrt{r}\cos\dfrac{\theta}{2}\left(2-2\nu-\cos^2\dfrac{\theta}{2}\right) \\ u_y(r,\theta) = \dfrac{2(1+\nu)}{\sqrt{2\pi}}\dfrac{K_{\mathrm{I}}}{E}\sqrt{r}\sin\dfrac{\theta}{2}\left(2-2\nu-\cos^2\dfrac{\theta}{2}\right) \\ \sigma_{xx}(r,\theta) = \dfrac{K_{\mathrm{I}}}{\sqrt{2\pi r}}\cos\dfrac{\theta}{2}\left(1-\sin\dfrac{\theta}{2}\sin\dfrac{3\theta}{2}\right) \\ \sigma_{yy}(r,\theta) = \dfrac{K_{\mathrm{I}}}{\sqrt{2\pi r}}\cos\dfrac{\theta}{2}\left(1+\sin\dfrac{\theta}{2}\sin\dfrac{3\theta}{2}\right) \\ \sigma_{xy}(r,\theta) = \dfrac{K_{\mathrm{I}}}{\sqrt{2\pi r}}\sin\dfrac{\theta}{2}\cos\dfrac{\theta}{2}\cos\dfrac{3\theta}{2} \end{cases}, \tag{84}$$

where $K_{\mathrm{I}} = \sigma\sqrt{\pi a}$ is the SIF corresponding to the mode I fracture.

Fig. 4 illustrates the convergence rate error of the present approach using the quadratic shape function versus the element size h. Note that h is defined by $h = \sqrt{2A_\Omega/N_e}$, where A_Ω is the area of the whole problem domain and N_e is the total number of elements in the whole problem domain. It can be observed that the precision provided by proposed approach is higher than other methods and the computational effect is decreased significantly. Fig. 5a shows the geometry deformation. Fig. 5b presents the contour plot of the stress σ_{yy}, which reveals that the maximum value is located around the crack tip.

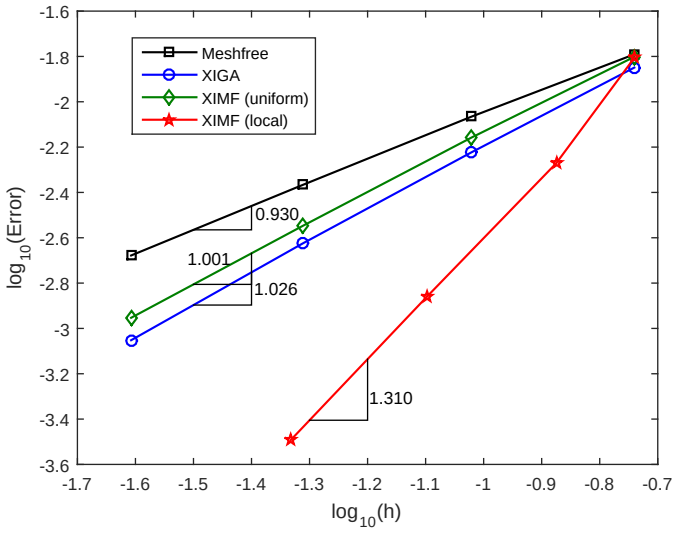

Figure 4: Convergence results of SIF for the mode I in terms of H_1 error norms.

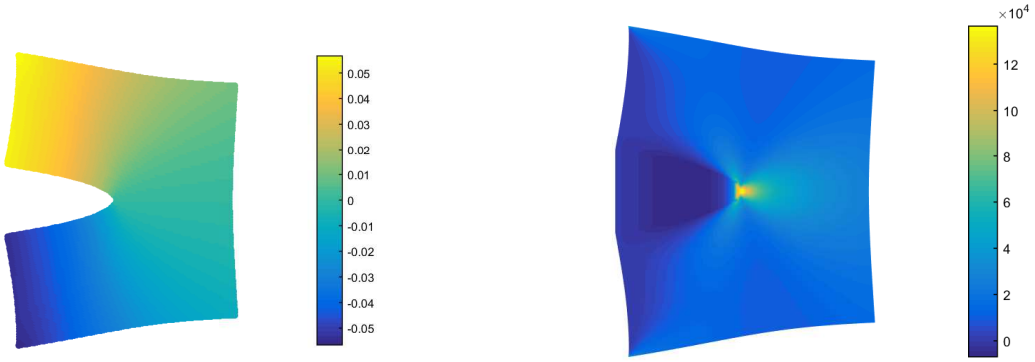

(a) (b)

Figure 5: (a) Geometry of deformation, and (b) contour plot of the stress σ_{yy}.

6.1.2. *Fracture in plates with out-of-plane bending*

The displacement fields around the crack tip for a plate undergoing the mode III fracture is investigated in this section. Fig. 6 presents a clamped plate which contains an edge crack and is subjected to two point loads in opposite directions with a magnitude $P = 0.1$KN. The geometry and material properties are listed as: width $b = 1$m, length $l = 2$m, Young's modulus $E = 1 \times 10^7$ KN/m^2 and Poisson's $\nu = 0.3$. Fig. 7 demonstrates the deformed shape and the shear stress component σ_{xy} of the plate in mode III. Fig. 8 shows the SIF versus the different crack lengths. The mode II SIF increases and reaches its maximum value at crack length ratio $a/b = 0.5$. Then the SIF decreases steadily with an increase in the crack length. It is obvious that the upper limit of the mode II SIF is affected by the crack length ratio.

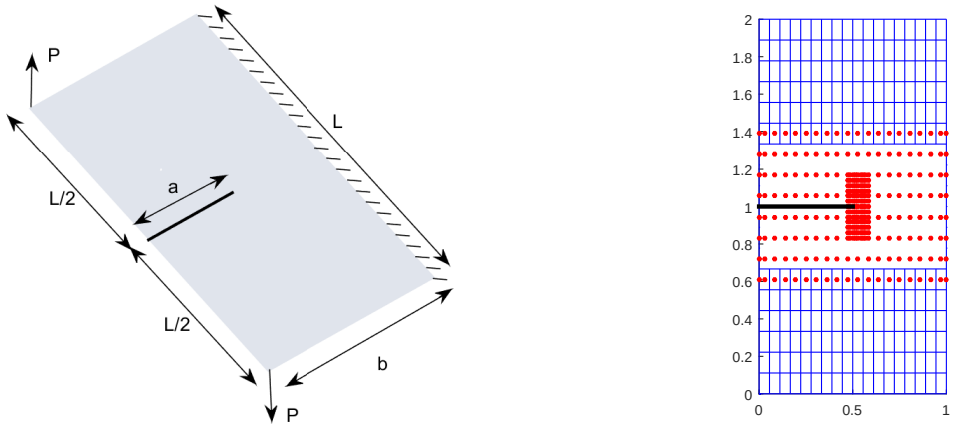

Figure 6: Geometry and boundary conditions of a plate in fracture mode 3 and the local refinement mesh.

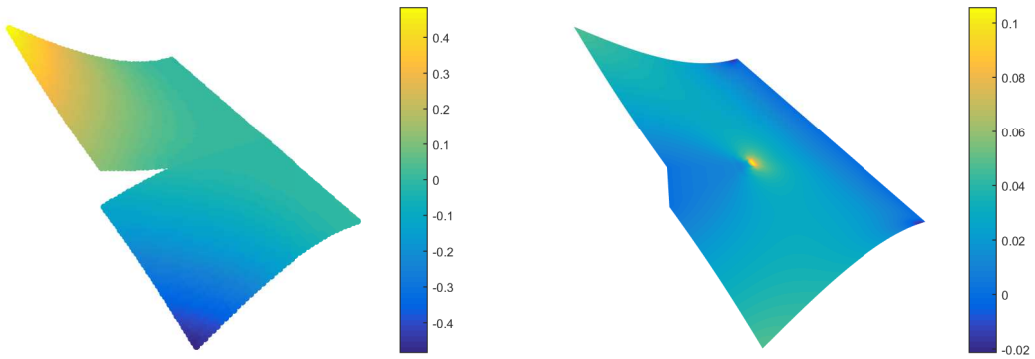

(a) (b)

Figure 7: (a) Deformed shape of the plate, and (b) the stress component σ_{xy}.

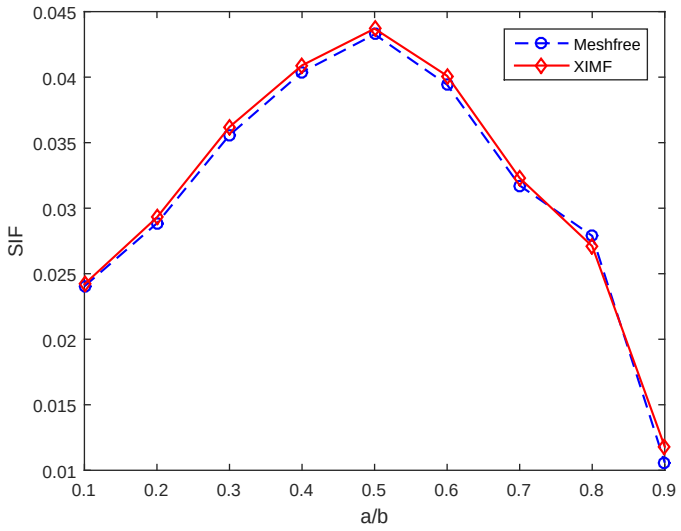

Figure 8: The SIF for different crack lengths.

6.1.3. Central cracked plate subjected to pressure loading

Consider a square plate with a central crack under uniform pressure (Fig. 9). The plate is simply supported on all edges. The geometry and material parameters are $b = 1.0$m, Young's modulus $E = 1 \times 10^7$ KN/m^2 , Poisson's $\nu = 0.3$, and pressure loading $p = 1 \times 10^4$ KN/m^2.

The results of the J-integral for various lengths of the central crack in two different cases of thickness, $b/h = 6$ and $b/h = 10$, are illustrated in Fig. 10. The results of the present approach are in good agreement with those presented by Sosa and Eischen[59].

The effect of different types of enrichment is presented in Fig. 11. Firstly, the SIFs are calculated with all enrichment functions (state 1). Next, the SIFs are calculated in the bending enrichment without the out-of-plane enrichment (state 2). Finally, the SIFs are calculated in the of out-of-plane enrichment without the bending enrichment (state 3). It can be seen that only a small difference exists between states 1 and 2, which can be attributed to the fact that the out-of-plane enrichment has little influence on the SIFs. The SIFs of mode I and II are affected by the bending enrichment, while the SIF of mode III is affected by the out-of-plane enrichment. It is also observed that the SIFs decrease with increasing crack length, due to the geometrically constrained boundary.

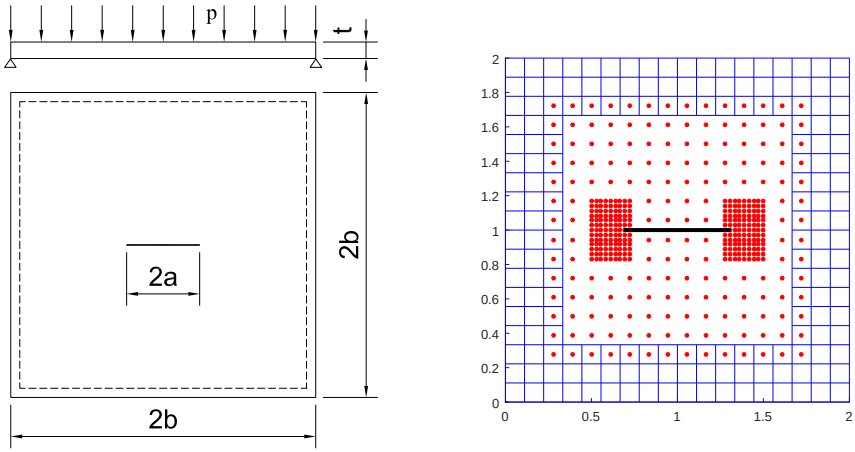

Figure 9: Geometry of a central cracked plate subjected to uniform pressure and the mesh.

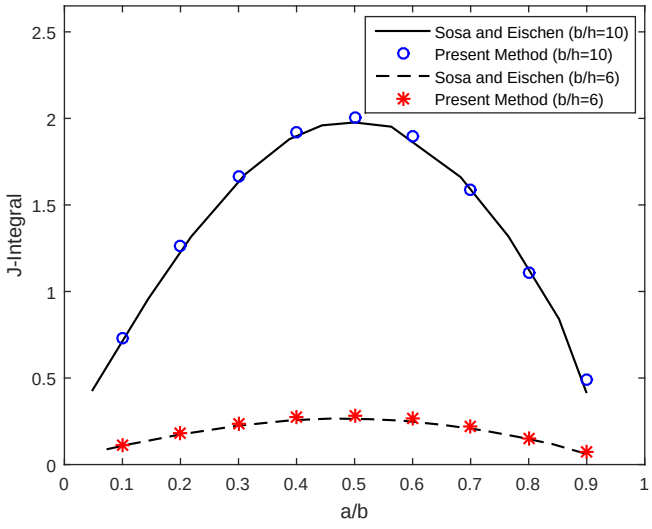

Figure 10: J-integral values of the central cracked plate subjected to uniform pressure.

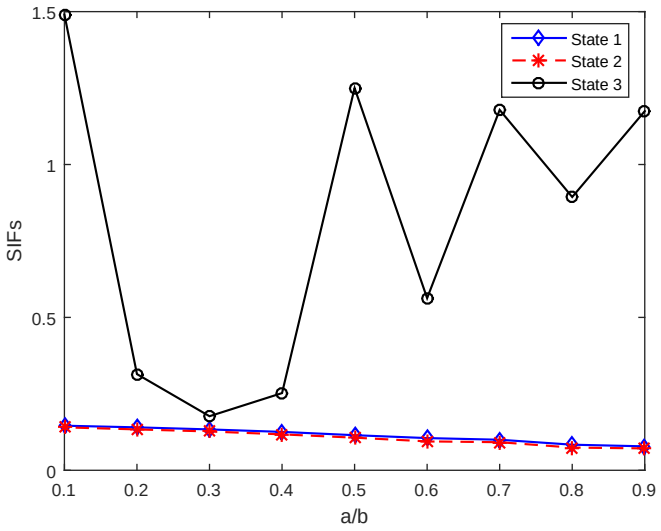

Figure 11: The SIF for different types of enrichments.

6.1.4. Pressurized cylindrical shell with an axial crack

Consider a cylindrical shell under internal pressure $p = 1 \times 10^4$ N/mm^2, radius $R = 20$mm and length $L = 100$mm, as illustrated in Fig. 12 . The material parameters are: Young's modulus $E = 1 \times 10^7$ N/mm^2 and Poisson's ratio $\nu = 0.3$. The crack length is normalized as

$$\rho = \frac{a}{\sqrt{Rt}} \tag{85}$$

where a is a half crack length and t is the thickness.

In order to show the accuracy of the present approach, the crack opening displacement in the middle of the crack is presented. The open-ended cylindrical shell with four different normalized crack lengths $\rho = 0.5, 1, 2, 3$ and four different values of $R/t = 5, 10, 20, 30$ are considered. Fig. 13 presents the displacement contours for different crack lengths ($R/t = 10$). Fig. 14 shows the comparison of the crack opening displacement obtained by the XIMF approach with the reference values presented by Huh et al.[60]. It is obvious that the obtained results are in good agreement with the reference solution.

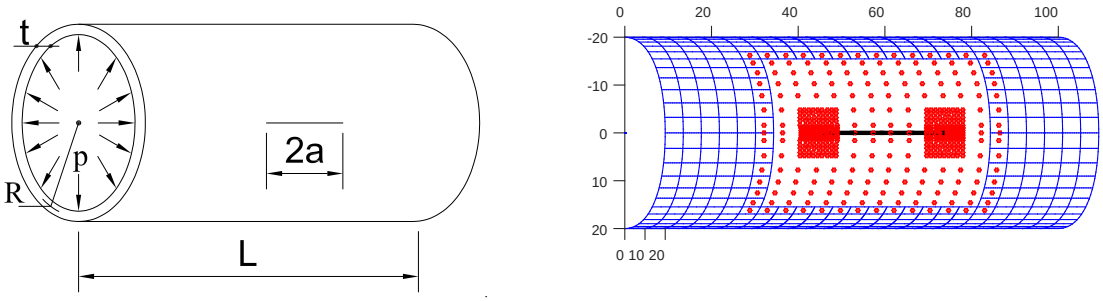

Figure 12: Geometry of a cylindrical shell under internal pressure with a longitudinal crack and the local refinement mesh.

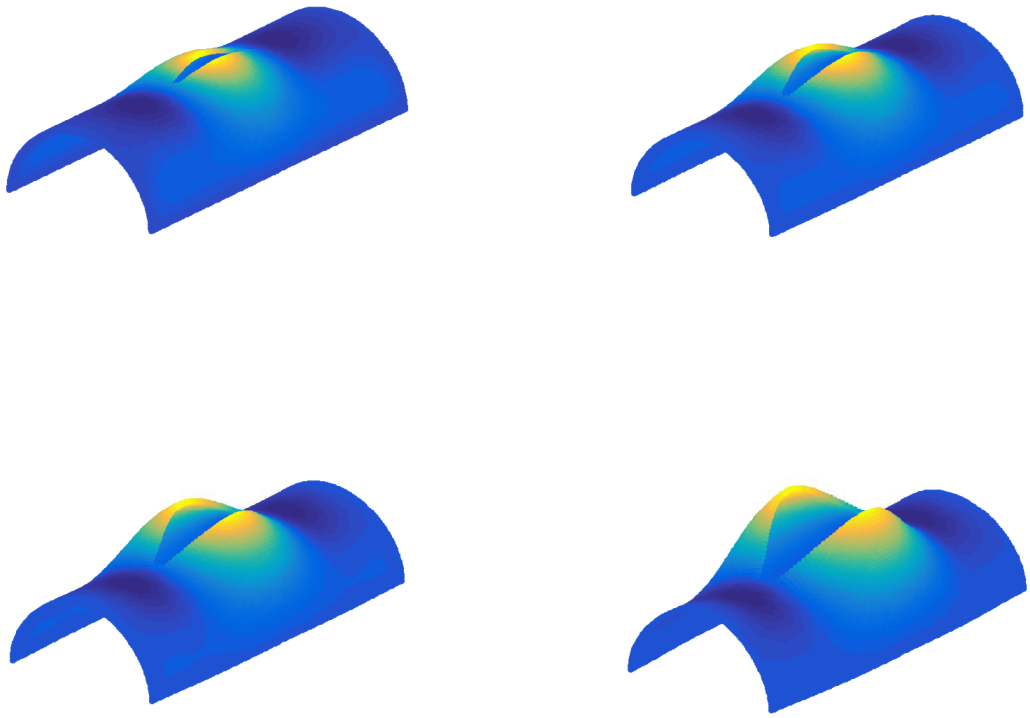

Figure 13: Displacements of a cylindrical shell with different crack lengths ($R/t = 10$).

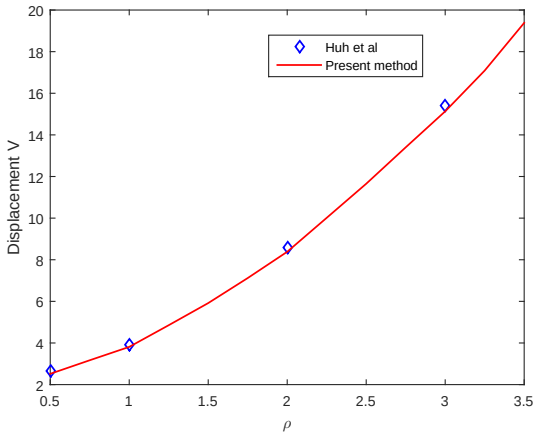

(a) $R/t = 5$

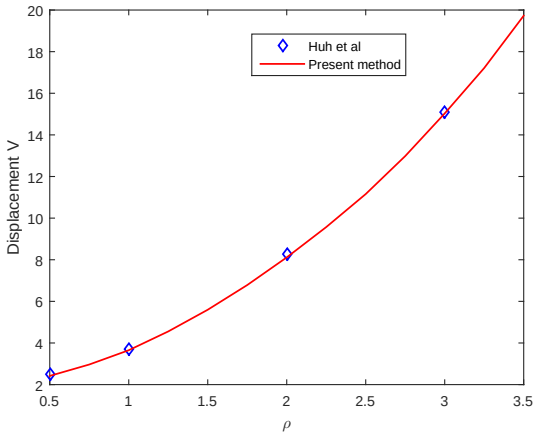

(b) $R/t = 10$

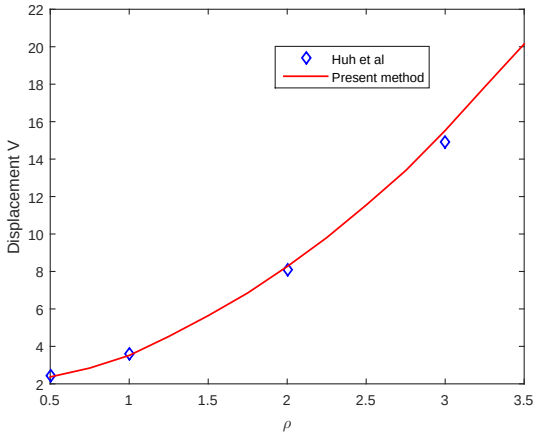

(c) $R/t = 20$

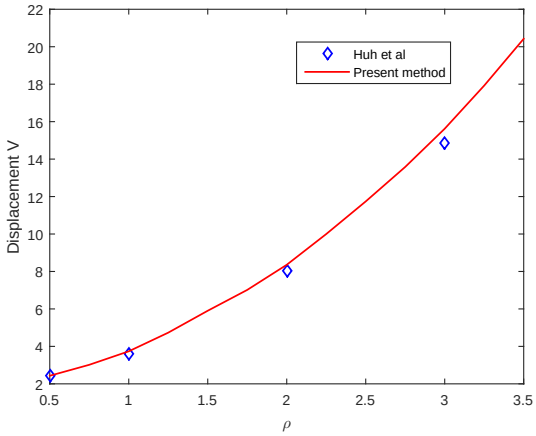

(d) $R/t = 30$

Figure 14: Comparison of crack opening displacements obtained by XIMF with the reference solution.

Table 1: The J-integral of circumferential crack cylindrical shell under tension loading.

		Methods				
2θ	R/t	Present method	Phantom[55]	Ref.[61]	Ref.[63]	Ref.[64]
45^o	6.2	4.225×10^{-4}	4.10×10^{-4}	4.56×10^{-4}	-	4.23×10^{-4}
	40	3.086×10^{-2}	3.03×10^{-2}	3.24×10^{-2}	3.09×10^{-2}	-
90^o	20	2.473×10^{-2}	2.40×10^{-2}	2.57×10^{-2}	2.48×10^{-2}	-

6.1.5. Cylindrical shell with a circumferential crack under tension

A thin cylindrical shell containing a circumferential through-wall crack which is located on the shell surface along the circular direction is considered. A pair of tensile forces $P = 90$N are applied on the cross section of the cylindrical shell in opposite directions (Fig. 15). The material parameters of the cylindrical shell are set as: Young's modulus $E = 2.07\times10^{11}$ N/mm^2 and Poisson ratio $\nu = 0.3$.

The contours of displacement on deformed configurations and stress component near the crack tips are shown in Fig. 16. Table 1 presents the J integral obtained by the proposed approach for different crack lengths. The results are in good agreement with the reference solutions [61] and analytical solutions reported in [62, 63].

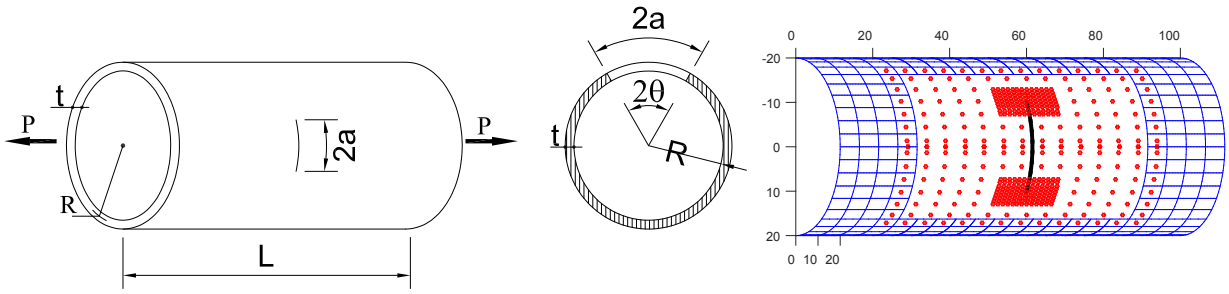

Figure 15: Geometry of a cylindrical shell under tension loading and the mesh.

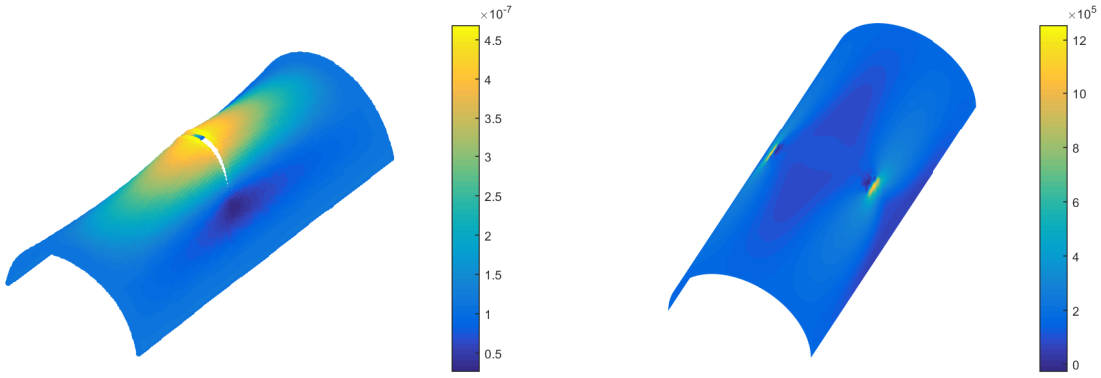

(a) (b)

Figure 16: Cylindrical shell containing a circumferential crack with the angle of 90^o under tension loading; (a) displacement field (deformation factor 2×10^4), and (b) stress component σ_{xx}.

6.1.6. Pressurized cylindrical shell with an inclined crack

A cylindrical shell with an inclined crack denoted by the angle θ is considered. The cylindrical shell is subjected to a uniform internal pressure $p = 10 \times 10^4$N and an axial tensile force $P = 8.8 \times 10^{-2}$N.

The displacement contour on deformed configurations is shown in Fig. 18. Contour plots of the force and moment components are shown in Fig. 19. Table 2 presents calculated J values for the cylindrical shell with the inclined crack at different angles α and various thicknesses of the cylindrical shell. The results obtained from the present approach are very close to the reference results. It can also be seen that the J value increases with the decreasing of the thickness.

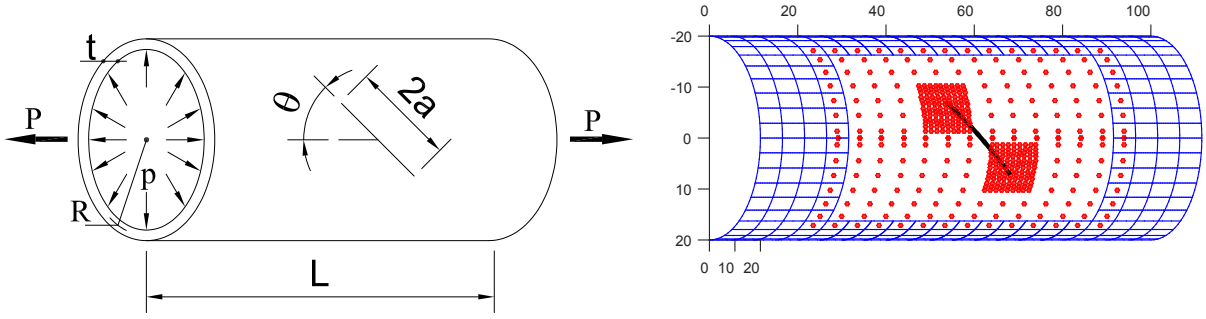

Figure 17: A cylindrical shell with a crack inclined at an angle α under uniform internal pressure and an axial tensile force and the mesh.

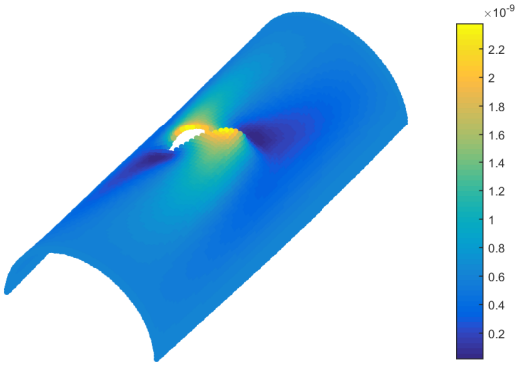

Figure 18: Deformation geometry of a pressurized cylindrical shell with a crack inclined at an angle $\alpha = 45^o$.

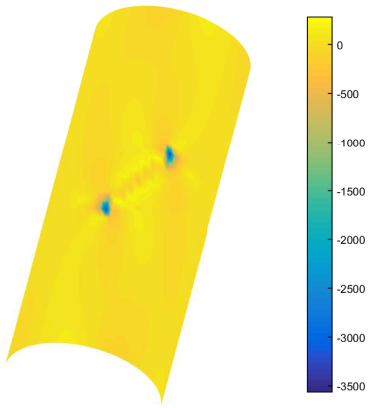

(a) Force N_{xx}

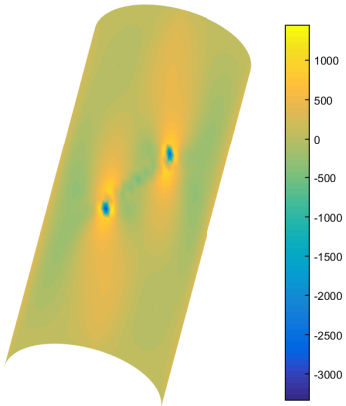

(b) Force N_{yy}

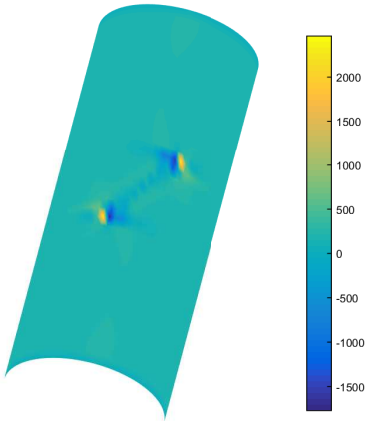

(c) Force N_{xy}

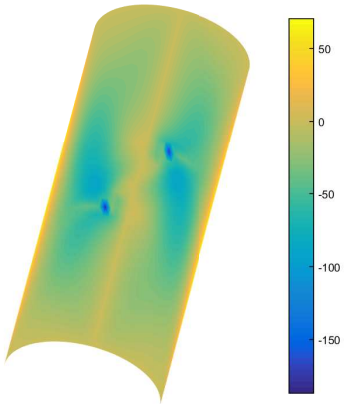

(d) Moment M_{xx}

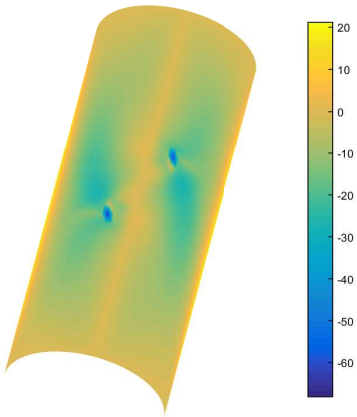

(e) Moment M_{yy}

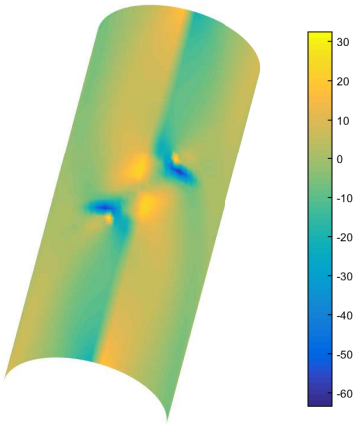

(f) Moment M_{xy}

Figure 19: Distribution of force and moment components of a pressurized cylindrical shell with an inclined crack $\alpha = 45^o$ and $R/t = 40$ (deformation factor 2×10^6).

Table 2: The J-integral of a pressurized cylindrical shell with variously inclined cracks.

R/t	Method	Scale	β(degree)				
			0	30	45	60	90
6.2	Present method	$\times 10^{-10}$	38.917	29.096	20.742	13.284	5.351
	XIGA[43]		38.743	28.726	20.534	12.972	5.246
	Phantom[55]		39.4	29.2	21.0	13.3	5.5
20	Present method	$\times 10^{-9}$	91.313	63.834	43.996	26.457	8.521
	XIGA[43]		91.164	63.453	43.768	25.912	8.347
	Phantom[55]		91.7	64.3	44.1	26.6	8.7
40	Present method	$\times 10^{-8}$	62.149	42.354	29.443	17.892	4.624
	XIGA[43]		61.875	42.041	28.946	17.673	4.425
	Phantom[55]		62.7	42.9	29.6	18.1	4.8

Table 3: Natural frequency coefficients of a support plate with the crack length $a/L = 0.4$.

Method	Mode					
	1	2	3	4	5	6
Present	18.281	46.533	49.028	78.579	85.414	98.678
Reference[65]	18.28	45.84	49.02	78.41	84.96	98.65
Reference[66]	18.28	46.62	49.03	78.60	85.51	98.68

6.2. Free vibration crack analysis

6.2.1. Square cracked plate

Consider a simply supported square plate with a central crack as shown in Fig. 9. The plate geometry and material are: length $L = 1$m, thickness $h = 0.1$m, mass density $\rho = 6000$ kg/m^3, Young's modulus $E = 2 \times 10^{11}$Pa and Poisson ratio $\nu = 0.3$. The crack lengths $a/L = 0.4$ and 0.8 are considered. The results are given in terms of a frequency parameter defined as $\lambda = \omega L^2 \sqrt{\rho h/D}$, where $D = Eh^3/(12(1-\nu^2))$. Fig. 20 shows the first six vibration mode shapes of the support plate, which demonstrate that the discontinuous deflection across the crack and highly smoothing approximation are invoked in the rest plate domain. Table 3 and Table 4 present the normalized natural frequencies for the support plate with different crack lengths. It can be seen that the obtained results are in good agreement with the reference solutions.

Table 4: Natural frequency coefficients of a support plate with crack length $a/L = 0.8$.

Method	Mode					
	1	2	3	4	5	6
Present	16.401	27.743	47.255	65.587	76.371	78.256
Reference[65]	16.40	26.71	47.23	64.39	76.36	77.96
Reference[66]	16.40	27.77	47.26	65.73	76.37	78.38

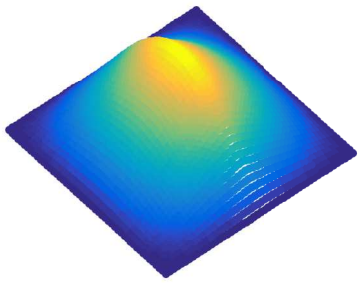

(a) Mode 1

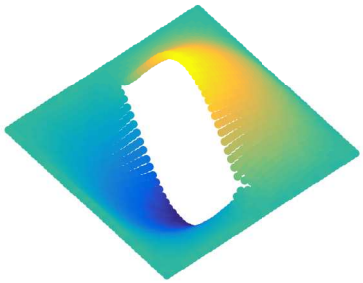

(b) Mode 2

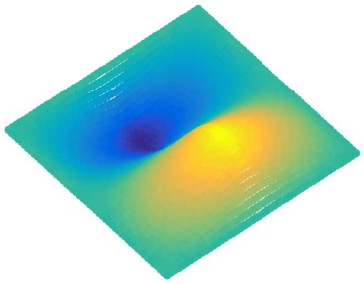

(c) Mode 3

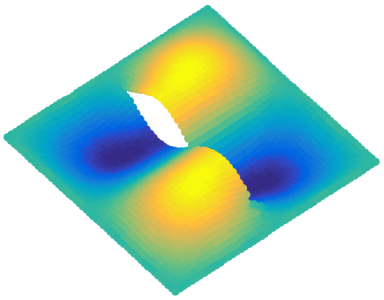

(d) Mode 4

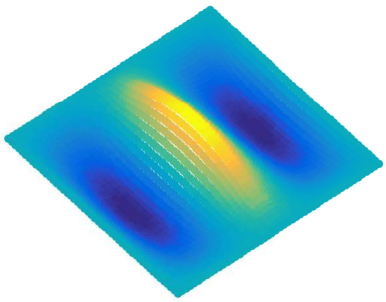

(e) Mode 5

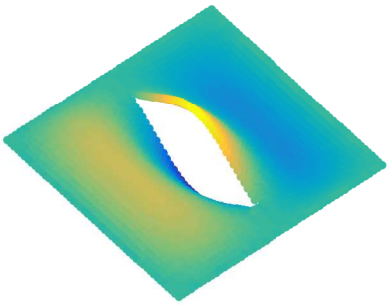

(f) Mode 6

Figure 20: The first six vibration mode shapes of a support plate with the crack length $a/L = 0.8$.

6.2.2. Cracked hemispherical panel

Last example, consider a hemispherical panel with center crack as shown in Fig. 21. The geometry and material are: radius $R = 1$m, thickness $t = 0.1$m, the Young's modulus $E = 2.1 \times 10^{11}$Pa, the Poisson's ratio $\nu = 0.3$, mass density $\rho = 7800$kg/m^3, and the crack length $a = 0.8$. The plot of comparison time results are shown Fig. 22. It can be found that the computation time of the proposed method is reduced considerably compare to the meshfree methods. The CPU time used by the coupling approach is 1087.3s, only 27.05% of that by meshfred method (1490.4s). Fig. 23 presents the first mode shapes for the hemispherical dome characterized by clamped-clamped-free-free boundary conditions. It is observed that highly smoothing transition of the vibration mode shapes can be achieved by the proposed method.

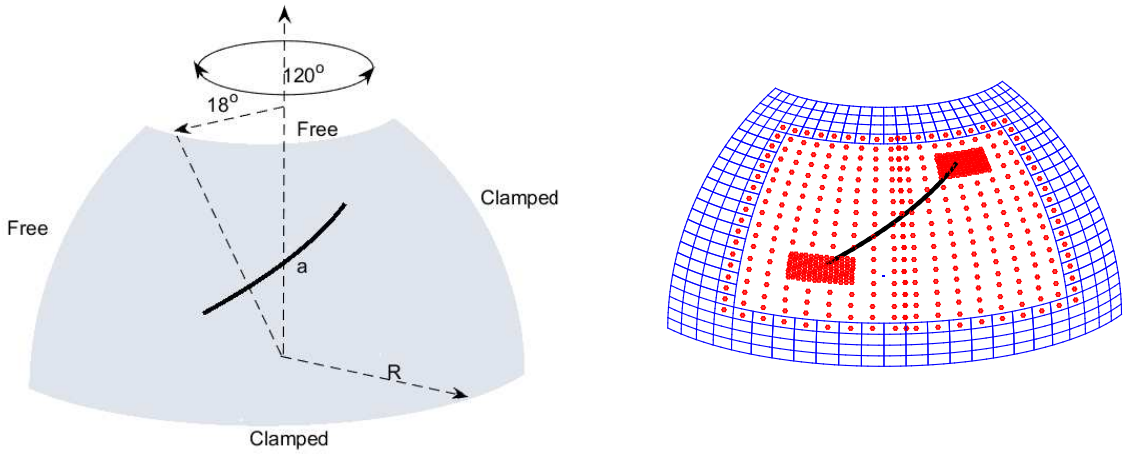

Figure 21: Geometry of a hemispherical panel with a center crack and the local refinement mesh.

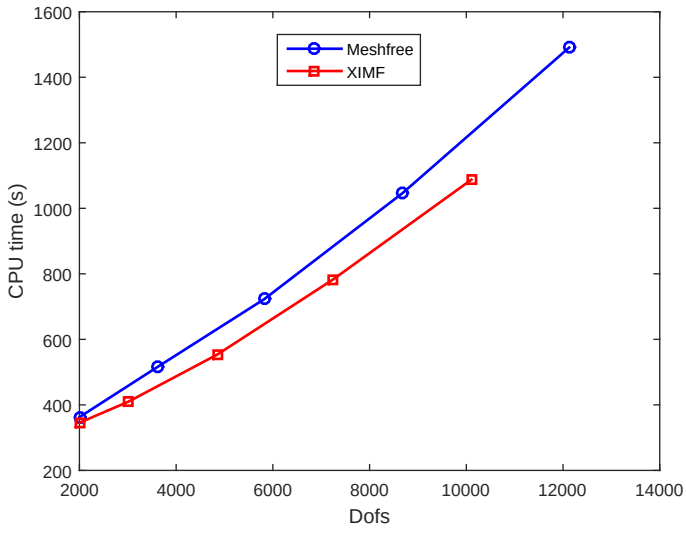

Figure 22: The comparison of computational cost.

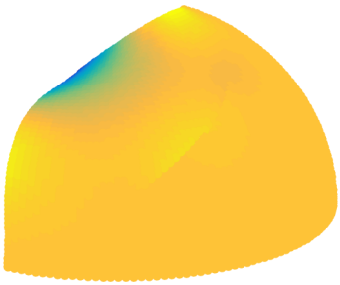

(a) Mode 1,ω= 37.6821(Hz)

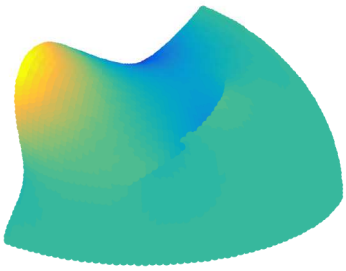

(b) Mode 2,ω= 45.5468(Hz)

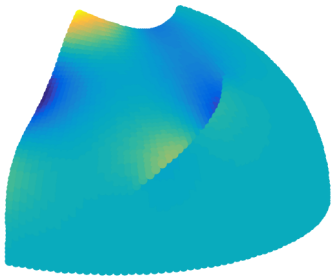

(c) Mode 3,ω= 88.0243(Hz)

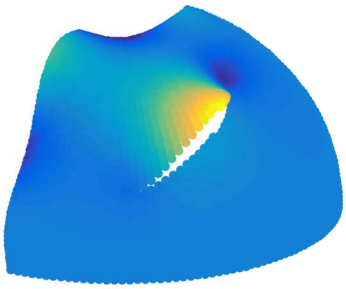

(d) Mode 4,ω= 97.1164(Hz)

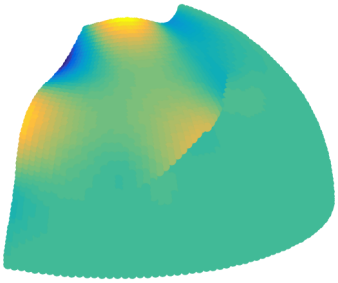

(e) Mode 5,ω= 124.2418(Hz)

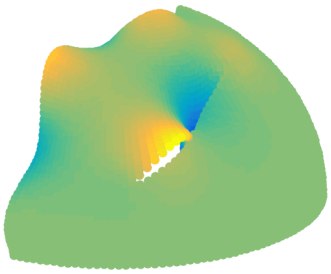

(f) Mode 6,ω= 132.7216(Hz)

Figure 23: The first six vibration mode shapes of the hemisphere panel.

7. Conclusions

In this paper, an XIMF coupling approach has been developed for the analysis of cracks in thin-shells based on the KL-theory. The present approach divides the physical domain into two sub-domains which are formulated with the IGA and meshfree methods, respectively. The meshfree is adopted in the sub-domain containing cracks, and the IGA basis functions are employed in areas away from cracks. Compared to the conventional meshfree and IGA methods, the present approach offers several advantages which are discussed below

- The present approach not only preserves the higher-order continuity and geometry exactness of the IGA but also keeps the ability of flexible local refinement by the meshfree method.
- The local refinement of the present approach can be incorporated quite easily compared to other IGA methods.
- The present approach can obtain a higher accuracy than traditional meshfree methods with the same model size or DOFs.
- The smooth transition between the two sub-domains is achieved by the consistency conditions, thus ensuring convergence of the present approach.
- The SIFs computed along the crack front are accurate by combining this approach with the high-order continuity in stress components.

Numerical results have been presented to demonstrate the effectiveness and accuracy of the coupling approach. However, the Gaussian integration of weak form is computational expensive in the meshfree sub-domain. A nodal integration method based on the Voronoi diagram will be investigated in the further research, which is able to avoid the mass calculation of the Gaussian integration.

Acknowledgments

This study is supported by the Singapore Maritime Institute (Grant No: SMI-2014-MA11) and the Ministry of Education, Singapore (Academic Research Fund, TIER 1-RG174/15).

Appendix A: Derivatives of strain variables

The membrane strains and bending strains can be expressed when second order derivatives of displacements are emitted

$$\delta\varepsilon_{\alpha\beta} = \frac{1}{2}\left(\delta\mathbf{u}_{,\alpha}\cdot\mathbf{G}_{\beta} + \delta\mathbf{u}_{,\beta}\cdot\mathbf{G}_{\alpha}\right),$$

$$\begin{aligned}\delta\kappa_{\alpha\beta} =& -\delta\mathbf{u}_{,\alpha\beta}\cdot\mathbf{G}_3 + \frac{1}{\bar{j}_0}\left(\delta\mathbf{u}_{,1}\cdot\left(\mathbf{G}_{\alpha,\beta}\times\mathbf{G}_2\right) - \delta\mathbf{u}_{,2}\cdot\left(\mathbf{G}_{\alpha,\beta}\times\mathbf{G}_1\right)\right)\\ &+ \frac{\mathbf{G}_{\alpha,\beta}\cdot\mathbf{G}_3}{\bar{j}_0}\left(\delta\mathbf{u}_{,1}\cdot\left(\mathbf{G}_2\times\mathbf{G}_3\right) + \delta\mathbf{u}_{,2}\cdot\left(\mathbf{G}_3\times\mathbf{G}_1\right)\right)\end{aligned}$$

The first derivative of membrane strains with respect to the nodal displacement u_r is given as follows:

$$\frac{\partial \varepsilon_{\alpha\beta}}{\partial u_r} = \frac{1}{2}\left(\mathbf{g}_\alpha \cdot \mathbf{g}_\beta - \mathbf{G}_\alpha \cdot \mathbf{G}_\beta\right)_{,r} = \frac{1}{2}\left(\mathbf{g}_{\alpha,r} \cdot \mathbf{g}_\beta + \mathbf{g}_\alpha \cdot \mathbf{g}_{\beta,r}\right).$$

The second derivative of membrane strains is calculated as

$$\frac{\partial^2 \varepsilon_{\alpha\beta}}{\partial u_r \partial u_s} = \frac{1}{2}\left(\mathbf{g}_{\alpha,r} \cdot \mathbf{g}_{\beta,s} + \mathbf{g}_{\alpha,s} \cdot \mathbf{g}_{\beta,r}\right).$$

The first derivative of the normal vector $\mathbf{g}_3$ with respect to the nodal displacement u_r is given as follows:

$$\mathbf{g}_{3,r} = \frac{\vec{\mathbf{g}}_{3,r}\bar{g}_3 - \vec{\mathbf{g}}_3\bar{g}_{3,r}}{\bar{g}_3^2} \quad , \quad \bar{g}_3 = |g_1 \times g_2| \quad , \quad \vec{\mathbf{g}}_3 = \mathbf{g}_1 \times \mathbf{g}_2,$$

where $\bar{g}_3$ represents the length of $\vec{\mathbf{g}}_3$, and the derivatives of $\bar{g}_{3,r}$ and $\vec{\mathbf{g}}_{3,r}$ are calculated:

$$\bar{g}_{3,r} = \frac{\vec{\mathbf{g}}_3\vec{\mathbf{g}}_{3,r}}{\bar{g}_3} \quad , \quad \vec{\mathbf{g}}_{3,r} = \mathbf{g}_{1,r} \times \mathbf{g}_2 \ + \mathbf{g}_1 \times \mathbf{g}_{2,r}.$$

The derivative of $\mathbf{g}_{\alpha,\beta}$ with respect to the nodal displacement u_r is given as follows:

$$\mathbf{g}_{\alpha,\beta,r} = \sum_{I=1}^{NS} \Phi_{I,\alpha\beta}(\xi)\, u_{I,r}.$$

The first derivatives of bending strains $\kappa_{\alpha\beta}$ with respect to the nodal displacement u_r can be given as follows:

$$\kappa_{\alpha\beta,r} = \left(\mathbf{G}_{\alpha,\beta} \cdot \mathbf{G}_3 - \mathbf{g}_{\alpha,\beta} \cdot \mathbf{g}_3\right)_{,r} = -\mathbf{g}_{\alpha,\beta,r} \cdot \mathbf{g}_3 - \mathbf{g}_{\alpha,\beta} \cdot \mathbf{g}_{3,r}.$$

The second derivatives of bending strains can be further obtained as follows:

$$\kappa_{\alpha\beta,rs} = \left(\mathbf{G}_{\alpha,\beta} \cdot \mathbf{G}_3 - \mathbf{g}_{\alpha,\beta} \cdot \mathbf{g}_3\right)_{,rs} = -\left(\mathbf{g}_{\alpha,\beta,r} \cdot \mathbf{g}_{3,s} + \mathbf{g}_{\alpha,\beta,s} \cdot \mathbf{g}_{3,r} + \mathbf{g}_{\alpha,\beta} \cdot \mathbf{g}_{3,rs}\right).$$

Appendix B: Asymptotic fields near a crack tip

B.1. In-plane enrichment

The displacement and membrane stress components at a crack tip can be expressed in polar coordinates (r,θ) as follows [67]:

$$\left\{\begin{array}{c} u_1 \\ u_2 \end{array}\right\} = \frac{K_I}{2\mu}\sqrt{\frac{r}{2\pi}}\left\{\begin{array}{c} \cos\frac{\theta}{2}\left(2\frac{1-\nu}{1+\nu} + 2\sin^2\frac{\theta}{2}\right) \\ \sin\frac{\theta}{2}\left(\frac{4}{1+\nu} - 2\cos^2\frac{\theta}{2}\right) \end{array}\right\} + \frac{K_{II}}{2\mu}\sqrt{\frac{r}{2\pi}}\left\{\begin{array}{c} \sin\frac{\theta}{2}\left(\frac{4}{1+\nu} + 2\cos^2\frac{\theta}{2}\right) \\ -\cos\frac{\theta}{2}\left(2\frac{1-\nu}{1+\nu} - 2\sin^2\frac{\theta}{2}\right) \end{array}\right\}$$

$$\left\{\begin{array}{c} \sigma_{11} \\ \sigma_{12} \\ \sigma_{22} \end{array}\right\} = \frac{K_I}{\sqrt{2\pi r}}\cos\frac{\theta}{2}\left\{\begin{array}{c} 1 - \sin\frac{\theta}{2}\sin\frac{3\theta}{2} \\ \sin\frac{\theta}{2}\cos\frac{3\theta}{2} \\ 1 + \sin\frac{\theta}{2}\sin\frac{3\theta}{2} \end{array}\right\} + \frac{K_{II}}{\sqrt{2\pi r}}\cos\frac{\theta}{2}\left\{\begin{array}{c} \sin\frac{\theta}{2}\left(2 + \cos\frac{\theta}{2}\cos\frac{3\theta}{2}\right) \\ cos\frac{\theta}{2}\left(1 - \sin\frac{\theta}{2}\sin\frac{3\theta}{2}\right) \\ \sin\frac{\theta}{2}\cos\frac{\theta}{2}\cos\frac{3\theta}{2} \end{array}\right\}$$

where $\mu = E/2(1+\nu)$ is the shear modulus.

B.2. Out-of-plane enrichment

The internal stress due to bending can be computed by [55]

$$\left\{ \begin{array}{c} \sigma_{rr} \\ \sigma_{r\theta} \\ \sigma_{\theta\theta} \end{array} \right\} = \frac{k_1}{\sqrt{2r}} \frac{x_3}{2h} \frac{1}{3+\nu} \left\{ \begin{array}{c} (3+5\nu)\cos\frac{\theta}{2} - (7+\nu)\cos\frac{3\theta}{2} \\ -(1-\nu)\sin\frac{\theta}{2} + (7+\nu)\sin\frac{3\theta}{2} \\ (5+3\nu)\cos\frac{\theta}{2} + (7+\nu)\cos\frac{3\theta}{2} \end{array} \right\}$$
$$+ \frac{k_2}{\sqrt{2r}} \frac{x_3}{2h} \frac{1}{3+\nu} \left\{ \begin{array}{c} -(3+5\nu)\sin\frac{\theta}{2} + (5+3\nu)\sin\frac{3\theta}{2} \\ (-1+\nu)\cos\frac{\theta}{2} + (5+3\nu)\cos\frac{3\theta}{2} \\ -(5+3\nu)\left(\sin\frac{\theta}{2} + \sin\frac{3\theta}{2}\right) \end{array} \right\}$$

$$\left\{ \begin{array}{c} \sigma_{r3} \\ \sigma_{\theta 3} \end{array} \right\} = \frac{1}{(2r)^{3/2}} \frac{h}{2} \frac{1}{(3+\nu)} \left[1 - \left(\frac{2x_3}{h} \right)^2 \right] \left\{ \begin{array}{c} -k_1 \cos(\theta/2) + k_2 \sin(\theta/2) \\ -k_1 \sin(\theta/2) + k_2 \cos(\theta/2) \end{array} \right\}$$

$$\sigma_{33} = 0$$

where x_3 is the out-of-plane component of the current coordinate vector. The out-of-plane displacement is given

$$u_3 = \frac{(2r)^{\frac{3}{2}}\left(1-\nu^2\right)}{2Eh(3+\nu)} \left\{ k_1 \left[\frac{1}{3}\left(\frac{7+\nu}{1-\nu} \right) \cos\frac{3\theta}{2} - \cos\frac{\theta}{2} \right] + k_2 \left[-\frac{1}{3}\left(\frac{5+3\nu}{1-\nu} \right) \sin\frac{3\theta}{2} + \sin\frac{\theta}{2} \right] \right\}$$

References

[1] T.J.R. Hughes and W.K. Liu. Nonlinear finite element analysis of shells: Part I. Three-dimensional shells. *Computer Methods in Applied Mechanics and Engineering*, 26:331–362, 1981.

[2] T.J.R. Hughes and W.K. Liu. Nonlinear finite element analysis of shells: Part II. Two-dimensional shells. *Computer Methods in Applied Mechanics and Engineering*, 27:167–181, 1981.

[3] M. Bischoff, K.-U. Bletzinger, W.A. Wall, and E. Ramm. *Models and Finite Elements for Thin-Walled Structures*. John Wiley and Sons, New York, 2004.

[4] K.J. Bathe and E. Dvorkin. Our discrete Kirchhoff and isoparametric shell elements for nonlinear analysis - An assessment. *Computers and Structures*, 16:89–98, 1983.

[5] P. Krysl and T. Belytschko. Analysis of thin shells by the element free Galerkin method. *International Journal of Solids and Structures*, 33(20-22):3057–3080, 1996.

[6] F. Cirak, M. Ortiz, and P. Schröder. Subdivision surfaces: A new paradigm for thin shell analysis. *International Journal for Numerical Methods in Engineering*, 47:2039–2072, 2000.

[7] L. Noëls and R. Radovitzky. A new discontinuous Galerkin method for Kirchhoff-Love shells. *Computer Methods in Applied Mechanics and Engineering*, 197:2901–2929, 2008.

[8] L. Chen, N. Nguyen-Thanh, H. Nguyen-Xuan, T. Rabczuk, S. Bordas, and G. Limbert. Explicit finite deformation analysis of isogeometric membranes. *Computer Methods in Applied Mechanics and Engineering*, 277:104–130, 2014.

[9] D. Wang and J.S. Chen. Locking-free stabilized conforming nodal integration for meshfree Mindlin-Reissner plate formulation. *Computer Methods in Applied Mechanics and Engineering*, 193:1065–1083, 2004.

[10] J.S. Chen and D. Wang. A constrained reproducing kernel particle formulation for shear deformable shell in cartesian coordinates. *International Journal for Numerical Methods in Engineering*, 68:151–172, 2006.

[11] P.-A. Ubach and E. Onate. New rotation-free finite element shell triangle accurately using geometrical data. *Computer Methods in Applied Mechanics and Engineering*, 199(5-8):383–391, 2010.

[12] N. Nguyen-Thanh, T. Rabczuk, H.Nguyen-Xuan, and S. Bordas. A smoothed finite element method for shell analysis. *Computer Methods in Applied Mechanics and Engineering*, 198(2):165–177, 2008.

[13] N. Nguyen-Thanh, C.Thai-Hoang, H.Nguyen-Xuan, and T.Rabczuk. A smoothed finite element method for the static and free vibration analysis of shells. *Journal of Civil Engineering and Architecture*, 4:17–29, 2010.

[14] S. Timoshenko and S. Woinowsky-Krieger. *Theory of Plates and Shells (2nd edn)*. McGraw-Hill, New York, 1959.

[15] T. Rabczuk, S.P. Xiao, and M. Sauer. Coupling of meshfree methods with finite elements: Basic concepts and test results. *Communications in Numerical Methods in Engineering*, 22:1031–1065, 2006.

[16] T. Rabczuk and G. Zi. A meshfree method based on the local partition of unity for cohesive cracks. *Computational Mechanics*, 39:743–760, 2007.

[17] T. Rabczuk and T. Belytschko. Cracking particles: A simplified meshfree methods for arbitrary evovling cracks. *International Journal for Numerical Methods in Engineering*, 61:2316–2343, 2004.

[18] T. Rabczuk and T. Belytschko. Adaptivity for structured meshfree particle methods in 2D and 3D. *International Journal for Numerical Methods in Engineering*, 63(11):1559–1582, 2005.

[19] V.P. Nguyen, T.Rabczuk, S.Bordas, and M.Duflot. Meshless methods: a review and computer implementation aspects. *Mathematics and Computers in Simulation*, 79:763–813, 2008.

[20] J.J Monaghan. Smoothed particle hydrodynamics. *Annual review of astronomy and astrophysics*, 30(1):543–574, 1992.

[21] T. Belytschko, Y.Y.Lu, and L.Gu. Element-free Galerkin methods. *International Journal for Numerical Methods in Engineering*, 37(2):229–256, 1994.

[22] W.K. Liu, S. Jun, and Y.F. Zhang. Reproducing kernel particle methods. *International Journal for Numerical Methods in Fluids*, 20(8-9):1081–1106, 1995.

[23] W.K. Liu, S.Jun, S.Li, J.Adee, and T.Belytschko. Reproducing kernel particle methods for structural dynamics. *International Journal for Numerical Methods in Engineering*, 38(10):1655–1679, 1995.

[24] J.S. Chen, C.Pan, and W.K.Liu C.T.Wu. Reproducing kernel particle methods for large deformation analysis of non-linear structures. *Computer Methods in Applied Mechanics and Engineering*, 139:195–227, 1996.

[25] W.K. Liu, S.Li, and T.Belytschko. Moving least-square reproducing kernel methods methodology and convergence. *Computer Methods in Applied Mechanics and Engineering*, 143:113–154, 1997.

[26] T. Rabczuk, P.Areias, and T.Belytschko. A meshfree thin shell method for non-linear dynamic fracture. *International Journal for Numerical Methods in Engineering*, 72(5):524–548, 2007.

[27] T. Rabczuk and P. Areias. A meshfree thin shell for arbitrary evolving cracks based on an extrinsic basis. 16(2), 2008.

[28] D. Qian and T.Eason and S.Li and W.K.Liu. Meshfree simulation of failure modes in thin cylinder subjected to combined loads of internal pressure and localized heat. *International Journal for Numerical Methods in Engineering*, 76:1159–1180, 2008.

[29] B. Ren and S. Li. Modeling and simulation of large-scale ductile fracture in plates and shells. *International Journal of Solids and Structures*, 49:2373–2393, 2012.

[30] T. J.R. Hughes, J.A. Cottrell, and Y. Bazilevs. Isogeometric analysis: CAD, finite elements, NURBS, exact geometry and mesh refinement. *Computer Methods in Applied Mechanics and Engineering*, 194:4135–4195, 2005.

[31] T.J.R. Hughes, A. Reali, and G. Sangalli. Efficient quadrature for NURBS-based isogeometric analysis. *Computer Methods in Applied Mechanics and Engineering*, 199:301–313, 2010.

[32] S. Lipton, J.A Evans, Y. Bazilevs, T. Elguedj, and T.J.R. Hughes. Robustness of isogeometric structural discretizations und severe mesh distortion. *Computer Methods in Applied Mechanics and Engineering*, 199:357–373, 2010.

[33] Y. Bazilevs, V.M. Calo, J.A. Cottrell, J.A. Evans T.J.R Hughes, S. Lipton, and M.A. Scottand T.W. Sederberg. Isogeometric analysis using T-splines. *Computer Methods in Applied Mechanics and Engineering*, 199:229–263, 2010.

[34] N. Nguyen-Thanh, H. Nguyen-Xuan, S. Bordas, and T. Rabczuk. Isogeometric finite element analysis using polynomial splines over hierarchical T-meshes. *Materials Science and Engineering*, 1:in press, 2010.

[35] N. Nguyen-Thanh, H. Nguyen-Xuan, S. Bordas, and T. Rabczuk. Isogeometric analysis using polynomial splines over hierarchical T-meshes for two-dimensional elastic solids. *Computer Methods in Applied Mechanics and Engineering*, 200(21-22):1892–1908, 2011.

[36] D. Schillinger, L. Dede, M.A. Scott, J.A. Evans, M.J. Borden, E. Rank, and T.J.R. Hughes. An isogeometric design-through-analysis methodology based on adaptive hierarchical refinement of NURBS, immersed boundary methods, and T-spline CAD surfaces. *Computer Methods in Applied Mechanics and Engineering*, 249-252:116–150, 2012.

[37] R.Kruse, N.Nguyen-Thanh, L.De Lorenzis, and T.J.R.Hughes. Isogeometric collocation for large deformation elasticity and frictional contact problems. *Computer Methods in Applied Mechanics and Engineering*, 296:73–112, 2015.

[38] N.Nguyen-Thanh, K.Zhou, X.Zhuang, P.Areias, H.Nguyen-Xuan, Y.Bazilevs, and T.Rabczuk. Isogeometric analysis of large-deformation thin shells using RHT-splines for multiple-patch coupling. *Computer Methods in Applied Mechanics and Engineering*, 316:1157–1178, 2017.

[39] P. Tan, N. Nguyen-Thanh, and K. Zhou. Extended isogeometric analysis based on Bézier extraction for an fgm plate by using the two-variable refined plate theory. *Theoretical and Applied Fracture Mechanics*, 89:127–138, 2017.

[40] D.J. Benson, Y. Bazilevs, E. De Luycker, M.-C. Hsu, M. Scott, T.J.R. Hughes, and T. Belytschko. A generalized finite element formulation for arbitrary basis functions: From isogeometric analysis to XFEM. *International Journal for Numerical Methods in Engineering*, 83:765–785, 2010.

[41] E. De Luycker, D.J. Benson, T. Belytschko, Y. Bazilevs, and M.C. Hsu. X-FEM in isogeometric analysis for linear fracture mechanics. *International Journal for Numerical Methods in Engineering*, 87:541–565, 2011.

[42] C.V. Verhoosel, M.A. Scott, R. de Borst, and T.J.R. Hughes. An isogeometric approach to cohesive zone modeling. *International Journal for Numerical Methods in Engineering*, 87:336–360, 2011.

[43] S.S. Ghorashi, N. Valizadeh, and S. Mohammadi. Extended isogeometric analysis for simulation of stationary and propagating cracks. *International Journal for Numerical Methods in Engineering*, 89:1069–1101, 2012.

[44] N.Nguyen-Thanh, N.Valizadeh, M.N.Nguyen, H.Nguyen-Xuan, X.Zhuang, P.Areias, G.Zi, Y.Bazilevs, L.De Lorenzis, and T.Rabczuk. An extended isogeometric thin shell analysis based on kirchhoff-love theory. *Computer Methods in Applied Mechanics and Engineering*, 284:265–291, 2015.

[45] N. Nguyen-Thanh and K. Zhou. Extended isogeometric analysis based on pht-splines for crack propagation near inclusions. *International Journal for Numerical Methods in Engineering*, 112:1777–1800, 2017.

[46] D. Wang and H. Zhang. A consistently coupled isogeometric-meshfree method. *Computer Methods in Applied Mechanics and Engineering*, 268:843–870, 2014.

[47] A. Rosolen and M. Arroyo. Blending isogeometric analysis and local maximum entropy meshfree approximants. *Computer Methods in Applied Mechanics and Engineering*, 264:95–107, 2013.

[48] N. Valizadeh, Y.Bazilevs, J.S.Chen, and T.Rabczuk. A coupled IGA-Meshfree discretization of arbitrary order of accuracy and without global geometry parameterization. *Computer Methods in Applied Mechanics and Engineering*, 293:20–37, 2015.

[49] H. Zhang and D. Wang. Reproducing kernel formulation of B-spline and NURBS basis functions: A meshfree local refnement strategy for isogeometric analysis. *Computer Methods in Applied Mechanics and Engineering*, 320:474–508, 2017.

[50] N. Nguyen-Thanh, H.Huang, and K.Zhou. An isogeometric-meshfree coupling approach for analysis of cracks. *International Journal for Numerical Methods in Engineering*, 113:1630–1651, 2018.

[51] D. Levin. The approximation power of moving least-squares. *Mathematics of Computation of the American Mathematical Society*, 67(224):1517–1531, 1998.

[52] G.R. Liu and Y.T. Gu. *An introduction to meshfree methods and their programming*. Springer Science & Business Media, 2005.

[53] N.T. Dung and G.N. Wells. Geometrically nonlinear formulation for thin shells without rotation degrees of freedom. *Computer Methods in Applied Mechanics and Engineering*, 197(33):2778–2788, 2008.

[54] T. Belytschko, W.K.Liu, B.Moran, and K.Elkhodary. *Nonlinear finite elements for continua and structures*. John Wiley & Sons, 2013.

[55] N. Moës, J. Dolbow, and T. Belytschko. A finite element method for crack growth without remeshing. *International Journal for Numerical Methods in Engineering*, 46:133–150, 1999.

[56] T. Chau-Dinh, G. Zi, P.S. Lee, T. Rabczuk, and J.H. Song. Phantom-node method for shell models with arbitrary cracks. *Computers and Structures*, 92-93:242–256, 2012.

[57] G.P. Nikishkov and S.N. Atluri. Calculation of fracture mechanics parameters for an arbitrary three-dimensional crack, by the "Equivalent Domain Integral" method. *International Journal for Numerical Methods in Engineering*, 24:1801–1821, 1987.

[58] F. Cirak, M.Ortiz, and P.Schroder. Subdivision surfaces: a new paradigm for thin-shell finite-element analysis. *International Journal for Numerical Methods in Engineering*, 47(12):2039–2072, 2000.

[59] H. Tada, P.C.Paris, and G.R.Irwin. *The Stress Analysis of Cracks Handbook*. ASME Press, New York, 2000.

[60] H.A. Sosa and J.W. Eischen. Computation of stress intensity factors for plate bending via a path-independent integral. *Engineering Fracture Mechanics*, 25:451–462, 1986.

[61] N.S. Huh, D.J.SHIM, S.CHOI, and K.B. PARK. Stress intensity factors and crack opening displacements for slanted axial through-wall cracks in pressurized pipes. *Fatigue and Fracture of Engineering Materials and Structures*, 31:428–440, 2008.

[62] P. Le Port, H.G. de Lorenzi, V. Kumar, and M.D. German. Virtual crack extension method for energy release rate calculations in flawed thin shell structures. *J. Press Vessel Technol ASME*, 109:101–107, 1987.

[63] E.S. Folias. On the effect of initial curvature on cracked flat sheets. *International Journal of Fracture Mechanics*, 5:327–346, 1968.

[64] Jr.J.L. Sander. Circumferential through-cracks in cylindrical shells under tension. *Journal of Applied Mechanics ASME*, 49:103–107, 1982.

[65] E.S. Folias. On the effect of initial curvature on cracked flat sheets. *International Journal Fracture Mechanics*, 5:327–346, 1969.

[66] H. Zhang, J.Wu, and D.Wang. Free vibration analysis of cracked thin plates by quasi-convex coupled isogeometric-meshfree method. *Frontiers of Structural and Civil Engineering*, 9:405–419, 2015.

[67] B. Stahl and L.M. Keer. Vibration and stability of cracked rectangular plates. *International Journal of Solids and Structures*, 8:69–91, 1972.

[68] A.T. Zehnder and M. J. Viz. Fracture mechanics of thin plates and shells under combined membrane, bending, and twisting loads. *Applied Mechanics Reviews ASME*, 58:37–48, 2005.